Frequency-Domain Modeling and Optimization of Graphene FET-based Molecular Communication Receivers

by

Ali Abdali

A Dissertation Submitted to the
Graduate School of Sciences and Engineering
in Partial Fulfillment of the Requirements for
the Degree of

Master of Science

in

Electrical and Electronics Engineering

KOÇ ÜNİVERSİTESİ

September 12, 2024

Frequency-Domain Modeling and Optimization of Graphene FET-based Molecular Communication Receivers

Koç University

Graduate School of Sciences and Engineering

This is to certify that I have examined this copy of a master's thesis by

Ali Abdali

and have found that it is complete and satisfactory in all respects,
and that any and all revisions required by the final
examining committee have been made.

Committee Members:

_____

Assist. Prof. Murat Kuşcu (Advisor)

_____

Assist. Prof. Levent Beker

_____

Prof. Barış Atakan

Date: _____

To my grandparents,

Mohammad Abdali and Begüm Abdali

ABSTRACT

Frequency-Domain Modeling and Optimization of Graphene FET-based Molecular Communication Receivers
Ali Abdali
Master of Science in Electrical and Electronics Engineering
September 12, 2024

Molecular Communication (MC) is a bio-inspired communication paradigm utilizing molecules for information transfer. Research on this unconventional communication technique has recently started to transition from theoretical investigations to practical testbed implementations, primarily harnessing microfluidics and sensor technologies. Developing accurate models for input-output relationships on these platforms, which mirror real-world scenarios, is crucial for assessing modulation and detection techniques, devising optimized MC methods, and understanding the impact of physical parameters on performance. In this thesis, we consider a practical microfluidic MC system equipped with a graphene field effect transistor biosensor (bioFET)-based MC receiver as the model system, and develop an analytical end-to-end frequency-domain model. The model provides practical insights into the dispersion and distortion of received signals, informing the design of new frequency-domain MC techniques, such as modulation and detection methods. The accuracy of the developed model is verified through particle-based spatial stochastic simulations of pulse transmission in microfluidic channels and ligand-receptor binding reactions on the receiver surface.

In the second part, I detail the fabrication and characterization of a graphene bioFET-based MC receiver. This micro/nanoscale receiver is integrated into a microfluidic channel and functionalized with a biorecognition layer composed of single-stranded DNA molecules-based receptors, designed to detect the target information molecules flowing through the fluidic channel. A *pre-equilibrium* detection method was explored to improve the data rate. The sensor's initial performance tests involved detection experiments with information encoded into ionic concentration. The fabricated MC receiver was electrically characterized in terms of transfer characteristics and hysteresis at each step of functionalization. The parasitic current

and mobility of the device is obtained. After functionalization with probe DNA, the receiver's time-varying response to concentration pulses of complementary target DNA was acquired with both fixed and varying pulse widths. Additionally, an intersymbol interference (ISI) analysis was conducted to evaluate the sensor's ISI performance. Finally, binary data transmission was performed using the MC setup, exploring various data rates and system parameters. The effects of key factors such as pulse width, symbol duration, flow velocity, and target DNA concentration were investigated. As such, this experimental work refined and optimized methodologies and designs from previous research, aiming at advancing practical MC techniques.

ÖZETÇE

Grafen FET Tabanlı Moleküler Haberleşme Alıcılarının Frekans-Bölgesi Modellemesi ve Optimizasyonu

Ali Abdali
Elektrik ve Elektronik Mühendisliği, Yüksek Lisans
12 Eylül 2024

Moleküler Haberleşme (MH), bilgi aktarımında molekülleri kullanan biyomimetik bir haberleşme paradigmasıdır. Bu alışılmadık haberleşme tekniği üzerine yapılan araştırmalar son dönemde teorik incelemelerden, mikroakışkanlar ve sensör teknolojilerinden faydalanan pratik test platformu uygulamalarına geçiş yapmıştır. Gerçek dünya senaryolarını yansıtan bu platformlarda giriş-çıkış ilişkileri için doğru modellerin geliştirilmesi, modülasyon ve algılama tekniklerinin değerlendirilmesi, optimize edilmiş MH yöntemlerinin oluşturulması ve fiziksel parametrelerin performans üzerindeki etkisinin anlaşılması açısından büyük önem taşımaktadır. Bu tezde, bir grafen alan etkili transistör biyosensörü (bioFET) tabanlı MH alıcısına sahip pratik bir mikroakışkan MH sistemi model olarak ele alınmış ve analitik bir uçtan uca frekans-alanı modeli geliştirilmiştir. Model, alınan sinyallerin dağılımı ve bozulması hakkında pratik içgörüler sağlayarak yeni frekans-alanı MH tekniklerinin, modülasyon ve algılama yöntemlerinin tasarımına katkıda bulunmaktadır. Geliştirilen modelin doğruluğu, mikroakışkan kanallarda atım iletiminin ve alıcı yüzeyindeki ligand-reseptör bağlanma reaksiyonlarının parçacık tabanlı uzamsal stokastik simülasyonları ile doğrulanmıştır.

İkinci bölümde, grafen bioFET tabanlı bir MH alıcısının üretimi ve karakterizasyonu üzerine yürütülen çalışmalar detaylandırılmaktadır. Bu mikro/nano ölçekli alıcı, bir mikroakışkan kanala entegre edilerek, sıvı kanalından geçen hedef bilgi moleküllerini tespit etmek amacıyla tek sarmallı DNA molekülleri tabanlı reseptörlerden oluşan bir biyo-tanıma katmanı ile fonksiyonelleştirilmiştir. Veri hızını artırmak için *denge-öncesi* (pre-equilibrium) bir algılama yöntemi araştırılmıştır. Sensörün ilk testleri, iyonik konsantrasyona dayalı algılama ile gerçekleştirilmiştir. Üretilen MH alıcısı, her fonksiyonelleştirme adımında transfer karakteristikleri ve histerezis açısından elektriksel olarak karakterize edilmiştir. Grafenin parazit akımı ve mo-

bilitesi elde edilmiştir. DNA reseptörler ile fonksiyonelleştirildikten sonra, sensörün zamana bağlı yanıtı, hem sabit hem de değişen atım genişliklerine sahip hedef DNA konsantrasyonu atımları kullanılarak elde edilmiştir. Ayrıca, sensörün semboller arası girişim (SAG) performansını değerlendirmek için bir SAG analizi yapılmıştır. Son olarak, çeşitli veri hızları ve sistem parametreleri incelenerek, MH düzeneği ile ikili (binary) veri iletimi gerçekleştirilmiştir. Atım genişliği, sembol süresi, akış hızı ve hedef DNA konsantrasyonu gibi anahtar faktörlerin etkileri incelenmiştir. Bu bağlamda, bu deneysel çalışma, önceki metodolojileri ve tasarımları optimize ederek, pratik MH tekniklerinin ilerlemesine katkı sağlamayı hedeflemiştir.

ACKNOWLEDGMENTS

I would like to express my deepest gratitude to my supervisor, Dr. Murat Kuşcu, for his invaluable support, guidance, and understanding throughout my MSc journey at Koç University. I am profoundly thankful for his trust in me and for offering me the opportunity to join the Calico group as a research assistant. His mentorship and encouragement have greatly influenced my academic and personal development, and I consider him a true role model.

I extend my sincere thanks to Dr. Levent Beker and Dr. Barış Atakan for serving on my thesis committee, for their critical reading of this thesis, and for their insightful suggestions and comments.

I am also deeply grateful to the members of the Calico group for their contribution and valuable collaborations. I would like to extend my especial thanks to Reza Sayyari and Amir Fathi for their invaluable support and encouragement. Furthermore, I owe immense gratitude to my family—my parents, MohammadHossein and Goli, my dear sister, Raziyeh, and my brother, Hamzeh—for their unconditional love and steadfast support. Had it not been for their unwavering support and commitment to my education, I would not have come this far. I also extend my heartfelt gratitude to my uncle Araz, my aunt Nahid, and my cousins Deniz and Elin. Their profound love and encouragement made this journey possible, and I could not have achieved this without them.

Lastly, I would like to express my gratitude to the National Scientific and Technological Council of Turkey (TÜBİTAK) for their financial support under Grant #120E301. I am also thankful to Koç University's Nanofabrication and Nanocharacterization Center for Scientific and Technological Advanced Research (N2STAR) for providing the infrastructure and training necessary to carry out the experimental aspects of this project.

Publications

Journal Papers

1. **Ali Abdali** and Murat Kuscu. Frequency-domain model of microfluidic molecular communication channel with graphene bioFET-based receiver. **IEEE Transactions on Communications (TCOM)**, published, 2024.

2. Iman Mokari Bolhassan, **Ali Abdali** and Murat Kuscu. Microfluidic molecular communication transmitter based on hydrodynamic gating. **IEEE Transactions on Molecular, Biological and Multi-Scale Communications (TMBMC)**, published, 2024.

3. **Ali Abdali**, M. K. Zadeh, I. M. Bolhassan, and M. Kuscu. Multiplexed signal transmission in a microfluidic molecular communication system with graphene bioFET-based receiver. **in preparation.**

4. A. S. Okcu, **Ali Abdali**, and M. Kuscu. Frequency-domain modeling of ligand-receptor systems linearized via Volterra series in molecular communications **in preparation.**

5. M. K. Zadeh, M. Uzun, **Ali Abdali**, A. Azmoudeh, and M. Kuscu. Graphene hall sensor based receivers for molecular communications with magnetic nanoparticles **in preparation.**

Conference Papers

1. Meltem Civas, **Ali Abdali**, Murat Kuscu, and Ozgur B Akan. Frequency-domain detection for molecular communications. **IEEE International Conference on Communications 2023 (ICC)**

TABLE OF CONTENTS

List of Tables **xii**

List of Figures **xiii**

Abbreviations **xvii**

Chapter 1: Introduction **1**

1.1 Nanoscale and Molecular Communications 1

1.2 Fundamental Contributions 2

1.3 Thesis Outline 2

Chapter 2: Frequency-domain model **4**

2.1 Introduction 4

2.2 End-to-End Frequency-Domain Model 7

2.2.1 Transfer Function of Microfluidic Propagation Channel 8

2.2.2 Transfer Function of the Ligand-Receptor Binding Process . . 12

2.2.3 Transfer Function of Graphene BioFET-based MC Receiver . 14

2.2.4 End-to-End Transfer Function and Output Current Spectrum 20

2.3 Numerical Results 21

2.3.1 Propagation Channel 24

2.3.2 Ligand-Receptor Binding Process 26

2.3.3 End-to-End Model 27

2.3.4 End-to-End Gain and Delay 28

2.3.5 Sampling Frequency 29

2.4 Conclusion 32

Chapter 3: Graphene bioFET-based Molecular Communication Receiver **33**

3.1 Introduction 33

3.2 Fabrication of MC Receiver 34

3.3 Ionic Concentration-based Detection 37

3.4 Functionalisation of GFET 40

3.5 Characterization of MC Receiver 41

3.6 Communication Performance 48

Chapter 4: Conclusion **58**

Bibliography **60**

LIST OF TABLES

2.1 Default Values of Simulation Parameters 24

LIST OF FIGURES

2.1 (a) 2D view of microfluidic propagation channel. Propagation of concentration signal from the transmitter, positioned at $x = x_t$, to the receiver, positioned at $x = x_r$, based on convection and diffusion is depicted. (b) Block diagram of microfluidic MC channel utilizing LR interactions in biorecognition layer of graphene bioFET-based MC receiver. 8

2.2 (a) Schematic of the graphene bioFET combined with the equivalent circuit. (b) Small-signal equivalent model of the graphene bioFET. . . 15

2.3 Transfer function ($G_m(f)$) of graphene bioFET composed of two different response regime: (i) CPE-dominant regime and (ii) Z_{CPE} current regime. 20

2.4 Smoldyn simulation environment: (a) A pulse concentration of ligands is released into the microfluidics MC channel. (b) The pulse around the MC receiver position, where ligands initiate interactions with receptors. The dispersion of the pulse signal occurs as a result of ligand diffusion. (c) Pulse signal approaches the channel end leaving behind ligands bound to receptors. 23

2.5 (a) The analytical and simulation results of time-domain channel response under varying pulse width. (b) Spectrum pulse concentrations signal with varying pulse width driven from analytical model and simulation results. 25

2.6 (a) Concentration of pulse signals with varying diffusion coefficient in time domain. (b) Spectrum of pulse concentration in a varying diffusion coefficient setting. 26

2.7 (a) Number of bound receptors for varying binding rate in time-domain. (b) Spectrum of number of bound receptors for varying binding rate 27
2.8 (a) Number of bound receptors for varying unbinding rate in time-domain. (b) Spectrum of the number of bound receptors for varying unbinding rate. 28
2.9 Spectrum of output current (end-to-end model) from analytical expression and simulation results (a) for varying pulse width PW, (b) for varying amplitude of input concentration pulse C_m. 29
2.10 (a) The end-to-end gain, $\Gamma(f)$, of MC system calculated using (2.38), and (b) end-to-end delay, $\tau(f)$, of MC system obtained using (2.39). . 30
2.11 Sampling frequency as a function of (a) pulse width, (b) diffusion coefficient, and (c) flow velocity. 31

3.1 Design of MC receiver using computer-aided for optical lithography. . 36
3.2 a) Optical micrograph of fabricated MC receiver after Al_2O_3 etching process. b) Closer look to area of a graphene channel in MC Receiver. c) MC receiver integrated with PDMS microfulidic channel. 37
3.3 a) Generation of 0.01xPBS pulses over a 1xPBS baseline. b) Pulse generation and detection using 0.1xPBS and 0.01xPBS with 1xPBS as the baseline. c) Waveforms consisting of 0.1xPBS and 0.01xPBS pulses with a constant pulse width of 60 seconds. 39
3.4 a) The molecular structure of PBASE, along with a schematic representation of probe DNA (pDNA) and its matching target DNA (tDNA). b) Noncovalent binding of PBASE to graphene through $\pi-\pi$ interactions. c) The attachment of pDNA through a conjugation process involving the succinimide group of PBASE. d) Hybridization of pDNA and tDNA. 40

3.5 a) Microfluidic MC setup consists of a pressure controller, a high-precision source-measure unit, a flow distributor, a flow sensor, electrical probes, and various microfluidic components. b) Closer look to fabricated MC receiver bonded with PDMS channel. c) Probe connection for applying/sensing electrical voltage/current. 42
3.6 The transfer characteristics of a GFET at various stages of functionalization, represented by the drain-to-source current (I_{ds}) as a function of varying gate potential (V_{gs}) with a sweep rate of 1 mV/s. In all measurements, the drain-to-source voltage (V_{ds}) is held constant at V_{ds} =100 mV. 44
3.7 Transfer curve measurements for different steps of functionalisation: (a) PBS, (b) PBASE, (c) pDNA, (d) Ethanolamine. 45
3.8 Leakage current from the electrolyte gate to the source contact in the sensor: a) without the insulating layer, and b) with the insulating layer. 46
3.9 Transfer characteristics of the four graphene channels were measured in a back-gate configuration, where the back-gate voltage (V_{bg}) was swept from 0 V to 40 V in the forward direction, with the drain-source voltage (V_{ds}) set at 100 mV. 47
3.10 Sensor response to tDNA at various concentrations ranging from 1 nM to 1 μM, with the response strength corresponding to the tDNA concentration. 48
3.11 a) Sensor response to 10 nM tDNA pulses with a constant pulse width of 1 ks, followed by a PBS duration of 1.8 ks after each tDNA pulse. b) Sensor response to 10 nM tDNA pulses with varying pulse widths, ranging from 1 ks to 32 s, and a constant PBS duration of 1.3 ks. . . 50
3.12 ISI analysis of the sensor using 10 nM tDNA pulses with a constant pulse width and varying PBS durations ranging from 600 s to 5 s. . 51

3.13 Data transmission cycles utilizing 10nM tDNA molecules, with one parameter varied at a time. 54
3.14 Data transmission cycles employing 100 nM tDNA molecules, with a single parameter varied at a time. 56
3.15 Data transmission cycles employing 100 nM tDNA molecules, with a single parameter adjusted at a time. 57

ABBREVIATIONS

MC	Molecular Communıcatıon
IoBNT	Internet of Bio-Nano Things
bioFETs	Field-Effect Transistor Biosensors
LR	Ligand-Receptor
LTI	Linear and Time-Invariant
FDE	Frequency-Domain Equalizer
ISI	Inter-Symbol Interference
PSD	Power Spectral Density
1D	One-Dimensional
2D	Two-Dimensional
FT	Fourier Transform
U	Unbound
B	Bound
EDL	Electrical Double Layer
CPE	Constant Phase Element
DOS	Density Of States
PWM	Pulse Width Modulation
SLG	Single-layer graphene
CVD	Chemical vapor deposition
ssDNA	Single-stranded DNA
RIE	Reactive ion etching
ALD	Atomic layer deposition
tDNA	Target DNA
pDNA	Probe DNA

PBASE	1-Pyrenebutyric acid N-hydroxysuccinimide ester
DMF	N,N-Dimethylformamide
DC	Direct-current
PBS	Phosphate buffered saline
CNP	Charge neutrality point
DI	Deionized
BER	Bit error rate

Chapter 1

INTRODUCTION

1.1 Nanoscale and Molecular Communications

Nanomachines are envisioned as fundamental operational units capable of executing simple tasks, paving the way for a wide range of practical real-world applications, including targeted drug delivery, microsurgery, biosensing, environmental monitoring, and intra-body health monitoring. While performing tasks individually poses serious limitations for nanomachines and inhibits their efficiency, connecting them and creating nanonetworks would significantly enhance their functionality and capabilities [Akan et al., 2016, Akyildiz et al., 2020, Akyildiz et al., 2008, Marzo et al., 2019, Akyildiz et al., 2011].

Communications at the nano- and micro-scales have been extensively investigated recently to form nanonetworks comprising nanomachines. Thanks to advancements in nanotechnology, which enable the miniaturization and fabrication of devices ranging from 1 to 100 nm, it is now possible to produce nanoantennas and nanosensors. Due to the stringent requirements of the application environments and the functional limitations of the nanoscale devices, such as minimal invasiveness, and limited energy, there is a need for innovative communication schemes. Molecular communication (MC), a bio-inspired communication paradigm that uses molecules as information carriers, stands out as a promising method for nanocommunications. The exceptional propertıse of MC - including biocompatibility, energy efficiency, and reliability in complex and dynamic physiological environments - hold promise for enabling seamless interactions between natural/synthetic cells and micro/nanoscale devices, known as bio-nano things. Within the emerging framework of the Internet of Bio-Nano Things (IoBNT), MC is anticipated to usher in a new

era of unparalleled healthcare and environmental applications at the intersection of information communication technologies, biotechnology, and nanotechnology.

This thesis addresses the physical layer challenges in implementing molecular communication. Specifically, we explore realistic communication techniques that ensure reliable and high-speed communication within nanonetworks, and examine the interface between biological and cyber units to study their seamless integration. In this direction, we developed the first end-to-end analytical model in the frequency domain for MC, encompassing the three main processes of communication: propagation, reception, and transduction.

1.2 Fundamental Contributions

The contributions of this thesis to the field of molecular communication are as follows:

- Develop and analysis of realistic analytical model for microfluidic molecular communication systems in frequency-domain.
- Develop first particle-based spatial stochastic simulation algorithm for molecular communications.
- Design and fabrication of graphene field effect transistor based receiver for molecular communications.
- Characterization of graphene field effect transistor biosensor
- Binary data transmission using the fabricated MC system in various the data rate and system parameters.

1.3 Thesis Outline

The thesis is organized as follows.

Chapter 2: In this chapter, for the first time in literature, we develop the end-to-end frequency-domain analytical model for microfluidic molecular communication channel with graphene bioFET-based receiver. The end-to-end MC system is divided into three sequential components: molecular propagation within the microfluidic channel, ligand-receptor interactions, and graphene FET-based receiver transductions. The mathematical relationships for each module are developed separately, allowing for the investigation of the individual impact of each module on the overall communication performance of microfluidic MC systems. The model provides insights into the distortion, dispersion, and attenuation of the transmitted signal, potentially informing novel frequency-domain MC techniques, such as modulation and detection. The accuracy of the model is validated through particle-based spatial stochastic simulations, showing a high degree of agreement between the analytical model and the simulation results.

Chapter 3: In this chapter, we focus on the fabrication and characterization of a microfluidic molecular communication system. This system includes a microfluidic channel integrated with a graphene field-effect transistor with a biorecognition layer of aptamer-based receptors, which serves as receiver in molecular communication system and detect information encoded in the concentration of molecules flowing through the fluidic channel. The nanofabrication process of graphene BioFETs includes the wet transfer of graphene onto a silicon/silicon oxide substrate, deposition of gold contacts, deposition of an Al_2O_3 insulator layer, integration of graphene with the microfluidic channel using O_2 plasma, and biofunctionalization of the graphene surface with DNA receptors. Characterization of the sensor is performed at every step of fabrication and functionalization, and data transmission results using the fabricated microfluidic setup are reported.

Chapter 2

FREQUENCY-DOMAIN MODEL

2.1 Introduction

Molecular Communications (MC) is a bio-inspired communication paradigm that uses molecules as information carriers [Akan et al., 2016]. The unique properties of MC, such as biocompatibility, energy efficiency, and reliability under complex and dynamic physiological conditions, are promising for enabling seamless interactions among natural/synthetic cells and micro/nanoscale devices, so-called bio-nano things. Through the emerging Internet of Bio-Nano Things (IoBNT) framework, MC is expected to usher in a new era of unparalleled healthcare and environmental applications at the intersection of information communication technologies, biotechnology, and nanotechnology [Akyildiz et al., 2015, Akyildiz et al., 2020].

MC research has predominantly focused on the development of theoretical channel models, modulation, detection and coding schemes, as well as the design of transmitter and receiver architectures [Kuscu et al., 2019, Jamali et al., 2019]. Recent progress in the field has facilitated the integration of experimental validations with theoretical studies, utilizing MC testbeds of varying scales and sophistication. Notably, some of these testbeds, due to their scalability to micro/nanoscales, have the potential to serve as an ideal link between theoretical frameworks and practical applications of MC. Microfluidics technology plays a pivotal role in these practical investigations, as it enables the testing of diverse MC channels while offering comprehensive control over system parameters, such as flow conditions and channel geometry. Moreover, microfluidic channels closely mimic blood vessels and other biological microenvironments, characterized by convection-diffusion-based molecular transport processes [Zadeh et al., 2023].

Integrating chemical sensors into microfluidic chips has augmented the utility

of these testbeds, with sensors acting as MC receivers that vary in material, geometry, and transduction processes. Among these, affinity-based field-effect transistor biosensors (bioFETs) have emerged as compelling MC receiver architectures due to their inherent signal amplification, miniaturization capabilities, and ligand receptor-based interfaces that provide control over selectivity and sensitivity, resembling biological cells performing molecular sensing. Graphene bioFETs have garnered particular attention owing to the graphene's flexibility, two-dimensional (2D) geometry, and capacity to be functionalized with various bioreceptors, including DNA aptamers and proteins [Civas et al., 2023b]. Initial investigations involving practical microfluidic MC systems equipped with graphene bioFET-based MC receivers have already unveiled crucial insights into the effects of convection, diffusion, ligand-receptor (LR) binding reactions, and receiver material properties on the MC performance [Kuscu et al., 2021].

Despite these developments, the majority of theoretical and practical studies still primarily focus on the time-domain aspects of MC systems. This can be attributed to the fundamentally distinct nature of the information carriers, i.e., discrete molecules, which lead to ambiguities and complications in defining carrier waves and frequencies for this unconventional communication technique. Additionally, the innate nonlinearity and time-variance of MC communication systems pose challenges to the adoption of frequency-domain techniques as widely-utilized tools in MC research. Nevertheless, when operating regimes can be characterized or approximated as linear and time-invariant (LTI), exploring the frequency-domain features of MC systems can yield crucial insights regarding channel characteristics, such as bandwidth, as well as dispersion and distortion of the transmitted signals. This approach also offers a deeper understanding of the impact of various system parameters on communication performance, including channel geometry, LR binding kinetics at the channel/receiver interface, and the electrical characteristics of the transducer channel within the receiver. Moreover, frequency-domain models can enable the adoption of sophisticated communication tools and methods from conventional EM, including transfer functions and filters, to optimize MC systems and develop new communication techniques, such as frequency-domain pulse-shaping,

modulation and detection techniques.

There has been a limited focus on frequency-domain analysis in MC. A notable contribution is the frequency-domain model for diffusion-based MC systems developed in [Pierobon and Akyildiz, 2010], which allows the determination of the end-to-end normalized gain and delay of the MC system as a function of frequency. In [Huang et al., 2021a], a frequency-domain equalizer (FDE) was proposed to address the inter-symbol interference (ISI) problem in MC. The transfer function of the MC channel, considering only diffusion-based transport, was derived in [Wang et al., 2014]. In our recent study [Civas et al., 2023a], we introduced a frequency-domain detection technique for MC to estimate the concentration of information molecules in the presence of interfering molecules, leveraging LR binding kinetics. This method employs the power spectral density (PSD) of binding noise, which exhibits unique properties for each molecule type, enabling the differentiation of information molecules from interferers in the frequency-domain.

In this study, we present an end-to-end frequency-domain system model for a microfluidic MC channel employing a graphene bioFET-based MC receiver with ligand receptors on its surface for detecting molecular messages carried by information molecules (i.e., ligands). We consider transmitted signals as finite-duration molecular concentration pulses. We partition the end-to-end MC system into three subsystems: (i) the microfluidic propagation channel, where ligand propagation is governed by convection and diffusion; (ii) the channel/receiver interface, where the receiver's surface receptors interact with propagating ligands; and (iii) the graphene bioFET-based receiver, which transduces the number of bound receptors into an output electrical current.

We employed a modular approach to derive the end-to-end transfer function, similar to that adopted in many modeling studies in the MC literature [Unluturk and Akyildiz, 2016, Pal et al., 2021, Pierobon and Akyildiz, 2010]. This approach allows for the probing of the individual impact of each functional component of the microfluidic MC system on the overall communication performance, thereby improving the generalizability of our study to various physical architectures of MC channels, channel-receiver interfaces, and receivers. For instance, it allows seamless integration

of different types of affinity-based receivers, such as mechanical transduction-based MC receivers, as proposed in [Aktas and Akan, 2022], into our model. By employing LTI approximations, we analyze each subsystem independently and derive their transfer functions. We then combine these to obtain the end-to-end MC system's transfer function. The developed frequency-domain model is validated through particle-based spatial stochastic simulations using *Smoldyn*, an open-source simulation framework [Andrews, 2017]. The simulation results show a strong agreement with the developed analytical frequency-domain model. We also examine the impact of various system parameters, such as pulse width of input signals, diffusion coefficient of ligands, and binding and unbinding rates of LR pairs, on the transfer function. Additionally, we leverage the developed model to determine the minimum sampling frequency for digitizing the output current by identifying the cutoff frequency and applying the Nyquist–Shannon theorem.

The remainder of this paper is organized as follows. Section 2.2 offers an in-depth analysis of the three key components of the microfluidic MC system, followed by the development of the end-to-end frequency-domain model, which is then utilized to obtain the output signal. Section 2.3 presents the simulation results intended to validate the developed model. Lastly, Section 2.4 delivers concluding remarks.

2.2 End-to-End Frequency-Domain Model

In this section, we present the derivation of the end-to-end frequency-domain model for the microfluidic MC system, depicted in Fig. 2.1(a). The system comprises a rectangular cross-section microfluidic channel in which molecular signals are uniformly transmitted across the cross-section of the channel inlet. The microfluidic channel is assumed to be open-ended, with a two-dimensional graphene bioFET-based biosensor serving as the receiver, positioned at the bottom of the channel without obstructing molecular propagation.

To establish the end-to-end model, transfer functions are derived for three subsystems: propagation of ligands within the microfluidic MC channel, LR binding interactions at the receiver surface, and molecular-to-electrical transduction process

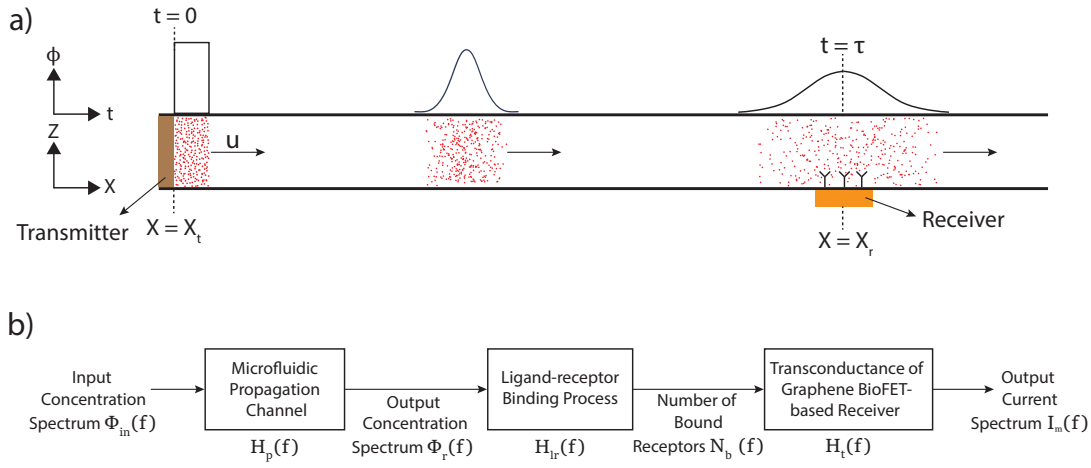

Figure 2.1: (a) 2D view of microfluidic propagation channel. Propagation of concentration signal from the transmitter, positioned at $x = x_t$, to the receiver, positioned at $x = x_r$, based on convection and diffusion is depicted. (b) Block diagram of microfluidic MC channel utilizing LR interactions in biorecognition layer of graphene bioFET-based MC receiver.

within the graphene bioFET-based MC receiver. The block diagram illustrating the end-to-end microfluidic MC system is provided in Fig. 2.1(b). This conceptual framework, characterized by their individual subsystems interconnected through input-output relationships, relies fundamentally on two key assumptions:

- The concentration of ligands in the vicinity of receptors is significantly greater than that of receptors.
- The rate at which ligands unbind from receptors is significantly greater than their binding rates.

2.2.1 Transfer Function of Microfluidic Propagation Channel

We consider a straight microfluidic channel with a rectangular cross-section which is filled up with an electrolyte as the medium of propagation for molecular signals. The transmitter is located at the entrance of the microfluidic channel, while the receiver, a graphene bioFET, is situated at the base of the channel at position $x = x_r$ as shown in Fig. 2.1(a). The surface of the graphene transduction channel of the receiver is

functionalized with selective receptors, which are exposed to ligands of time-varying concentration. The receiver senses the concentration of ligands, flowing over its surface, through LR binding reactions. The flow is unidirectional from the inlet to the open outlet of the microfluidic channel. Here, we consider the concentration of ligands far exceeding that of receptors, minimizing the impact of LR interaction on propagating ligand concentration. Therefore, we can safely neglect the concentration gradient formed near the receptors, as will be later justified through particle-based simulations in Section 2.3.

The convection-diffusion equation, which is a linear partial differential equation, describes the behavior of mass transport of ligands within the microfluidic channel as [Kuscu and Akan, 2018]

$$\frac{\partial \phi}{\partial t} = -u\nabla\phi + D\nabla^2\phi \tag{2.1}$$

where ϕ is the concentration of the released ligands, D is the diffusion coefficient of the ligands, u is the fluid flow velocity. The convection-diffusion equation describes the spatiotemporal evolution of the ligand concentration profile, ϕ, through the convective term ($-u\nabla\phi$) and the diffusive term ($D\nabla^2\phi$). As ligands propagate through convection-diffusion within an ionic medium, there is ionic screening in the surrounding medium, as shown in Fig. 2.2(a). The range of the electrostatic force is determined by the Debye length, which is inversely proportional to the square root of the ionic strength. This screening effect effectively diminishes the electrostatic force between charged ligands [Stylianopoulos et al., 2010, Chazalviel, 1999, Lindgren et al., 2019]. Therefore, given the relatively high ionic strength in our study, we have excluded the electrostatic force between these charged ligands from our analysis.

In this study, we consider a uniform and unidirectional fluid flow solely along the x-axis, i.e., $u = u_x$. To simplify the analysis of ligand transport, we adopt a one-dimensional (1D) approximation, focusing primarily on the x-axis. This assumption is justified when the ligand propagation is predominantly unidirectional, and lateral dispersion is much smaller than longitudinal transport. Such conditions arise due

to the design and flow characteristics of the microfluidic channel, as discussed in [Bicen and Akyildiz, 2013]. The validity of this approximation can be quantified using the Péclet number, defined as $Pe = u_x l/D$. In this definition, l denotes the characteristics length, and for our case, corresponds to the distance between the transmitter and the receiver, i.e., $l = x_r$. When $Pe \gg 1$, the 1D approximation is valid, which is consistent with the model parameter values considered in this study. Accordingly, the 1D solution of (2.1) for an input concentration signal in the form of an impulse at the origin (i.e., $\phi_{\text{in}}(x,t) = \delta(x - x_0, t - t_0)$ with $x_0 = 0, t_0 = 0$), gives the impulse response of the microfluidic propagation channel:

$$h_{\text{p}}(x,t) = \frac{1}{\sqrt{4\pi Dt}} \exp\left(-\frac{(x - u_x t)^2}{4Dt}\right). \tag{2.2}$$

The propagation delay, τ, is the time it takes for the peak ligand concentration to travel a distance of x from the channel inlet, given by $\tau = \frac{x}{u_x}$ for $Pe \gg 1$. The received concentration, ϕ_{r}, in the time-domain for an input concentration of ϕ_{in} in a straight microfluidic MC channel can be calculated through the convolution of the input concentration and the impulse response as follows:

$$\phi_{\text{r}}(l,t) = h(l,t) * \phi_{\text{in}}(l,t) = \int_{-\infty}^{+\infty} h_{\text{p}}(x,t)\phi_{\text{in}}(l - x)dx. \tag{2.3}$$

Here, a rectangular signal is preferred as input, commonly chosen in MC systems for its suitability in modulation and demodulation schemes, such as pulse width modulation (PWM), particularly in practical microfluidic systems [Kuscu et al., 2021, Deng et al., 2017, Bolhassan et al., 2023, Zadeh et al., 2023, Walter et al., 2023]. For a rectangular finite-duration concentration pulse input with a pulse width of T_p and amplitude of C_m, the received concentration at $x = l$ can be calculated using (2.3) as follows:

$$\phi_{\text{r}}(l,t) = \frac{C_m}{2}\left(\text{erf}\left(\frac{tu - l + T_p u}{2\sqrt{Dt}}\right) - \text{erf}\left(\frac{tu - l}{2\sqrt{Dt}}\right)\right). \tag{2.4}$$

The transfer function of the propagation channel, which represents the frequency response to an impulse signal, can be derived by solving the frequency-domain counterpart of the 1D convection-diffusion equation (2.1) obtained using the Fourier

Transform (FT):

$$j2\pi f\Phi(x,f) = -u\frac{\partial\Phi(x,f)}{\partial x} + D\frac{\partial^2\Phi(x,f)}{\partial x^2}, \tag{2.5}$$

where, $\Phi(x,f)$, the spectral density of ligand concentration, is obtained by taking the FT of the time-domain ligand concentration signal, i.e., $\Phi(x,f) = \mathcal{F}(\phi(x,t))$ [Bicen and Akyildiz, 2013]. Assuming $|(8\pi fD)/u^2| < 1$ to have a converging series expansion in solution of (2.5), and fixing $x = x_r$, the receiver's central position, we can analytically approximate the transfer function of the microfluidic propagation channel, i.e., $H_{\mathrm{p}}(f)$, as follows [Bicen and Akyildiz, 2013]

$$\begin{aligned} H_{\mathrm{p}}(f) &= H_{\mathrm{p}}(x = x_r, f) \\ &\approx \exp\left(-\left(\frac{(2\pi f)^2 D}{u^3} + j\frac{2\pi f}{u}\right)x_r\right). \end{aligned} \tag{2.6}$$

Spectral density of the received concentration, $\Phi_{\mathrm{r}}(f) = \Phi(x = x_r, f)$, can be obtained via multiplication of the transfer function, $H_{\mathrm{p}}(f)$, and the spectral density of the input ligand concentration signal, $\Phi_{\mathrm{in}}(f) = \Phi_{\mathrm{in}}(x = 0, f)$, as follows

$$\Phi_{\mathrm{r}}(f) \approx H_{\mathrm{p}}(f)\Phi_{\mathrm{in}}(f). \tag{2.7}$$

Note that the spectral density of a rectangular finite-duration concentration pulse input signal with amplitude C_m and pulse width T_p can be obtained by taking FT as

$$\Phi_{\mathrm{in}}(f) = \mathcal{F}\big\{C_m \mathrm{rect}(t/T_p - 0.5)\big\} = C_m T_p \,\mathrm{sinc}\,(fT_p), \tag{2.8}$$

where $\mathrm{rect}(t) = 1$ for $-0.5 < t < 0.5$ is the rectangular function. Therefore, combining (2.6), (2.7), and (2.8), spectral density of the received ligand concentration signal can be approximated as follows:

$$\Phi_{\mathrm{r}}(f) \approx \; C_m T_p \,\mathrm{sinc}\,(fT_p) \exp\left(-\left(\frac{(2\pi f)^2 D}{u^3} + j\frac{2\pi f}{u}\right)x_r\right). \tag{2.9}$$

Using (2.6), we can obtain the normalized gain and delay for the propagation process. The normalized gain $\Gamma_{\mathrm{p}}(f)$ for the propagation process is the magnitude of

the transfer function $|H_{\mathrm{p}}(f)|$ normalized by its maximum value $\max_{\mathrm{f}}(|H_{\mathrm{p}}(f)|)$ given as

$$\Gamma_{\mathrm{p}}(f) = \frac{|H_{\mathrm{p}}(f)|}{\max_{\mathrm{f}}(|H_{\mathrm{p}}(f)|)} = \exp\left(-\frac{(2\pi f)^2}{u^3} x_{\mathrm{r}}\right). \tag{2.10}$$

The delay of propagation module $\tau_{\mathrm{p}}(f)$ is

$$\tau_{\mathrm{p}}(f) = -\frac{d\varphi_{\mathrm{p}}(f)}{df} = \frac{2\pi x_{\mathrm{r}}}{u}, \tag{2.11}$$

where $\varphi_{\mathrm{p}}(f)$ is the phase of $H_{\mathrm{p}}(f)$ and given by

$$\varphi_{\mathrm{p}}(f) = \arctan\left(\frac{\mathrm{Im}(H_{\mathrm{p}}(f))}{\mathrm{Re}(H_{\mathrm{p}}(f))}\right). \tag{2.12}$$

For the propagation process, the normalized gain in (2.10) represents how the signal is attenuated while propagating through the microfluidic channel. The delay of this process in (2.11) represents the distortion effect during the time required for this propagation.

2.2.2 Transfer Function of the Ligand-Receptor Binding Process

Propagating ligands encoding information bind to the receptors on the graphene bioFET-based MC receiver surface randomly and reversibly such that a formed LR complex dissociates after a random time duration. In the case of a monovalent reaction, where receptors have only one binding site and can be in one of the two states, unbound (U) or bound (B), the reversible LR binding interactions can be described in terms of reaction rates as follows

$$\mathrm{U} \underset{\mathrm{k}_-}{\overset{\phi_r(\mathrm{t})\,\mathrm{k}_+}{\rightleftharpoons}} \mathrm{B}, \tag{2.13}$$

where k_+ and k_- are the binding and unbinding rates of the LR pair, and $\phi_{\mathrm{r}}(t)$ is the time-varying ligand concentration in the vicinity of receptors [Kuscu and Akan, 2019], assuming that receptors are exposed to the same ligand concentration at all times, and the number of ligands bound to receptors is much lower than the number of ligands in the vicinity of the receptors such that the ligand concentration $\phi_{\mathrm{r}}(t)$ can be assumed to remain unchanged during the LR binding interactions. The number of bound receptors as a function of time, i.e., $N_{\mathrm{b}}(t)$, can then be written as

$$\frac{dN_{\mathrm{b}}(t)}{dt} = k_+(N_r - N_{\mathrm{b}}(t))\phi_{\mathrm{r}}(t) - k_- N_{\mathrm{b}}(t), \tag{2.14}$$

where N_r is the total number of receptors on the receiver surface. The second-order reaction represented by the above nonlinear equation can be simplified as a first-order reaction, if the total number of receptors is much higher than the number of bound receptors at all times [Lauffenburger and Linderman, 1996]. This condition is met when the unbinding rate is sufficiently high, such that the ligand remains in the bound state for a short duration. In almost all living cells $k_+ \ll k_-$ [ShahMohammadian et al., 2013]. Here, we consider $k_+\phi_\mathrm{r}(t) \ll k_-$, ensuring the number of bound receptors is comparatively low with a high unbinding rate constant, yielding a linear equation:

$$\frac{dN_\mathrm{b}(t)}{dt} = k_+ N_r \phi_\mathrm{r}(t) - k_- N_\mathrm{b}(t). \tag{2.15}$$

The condition of first-order reaction can be quantitatively formulated as $k_+\phi_\mathrm{r}(t) \ll k_-$ [ShahMohammadian et al., 2013], ensuring the number of bound receptors is comparatively low with a high unbinding rate. The transfer function of the LR binding process can then be obtained by solving the frequency-domain equivalent of (2.15):

$$j2\pi f N_\mathrm{b}(f) = k_+ N_r \Phi_\mathrm{r}(f) - k_- N_\mathrm{b}(f), \tag{2.16}$$

considering $\Phi_\mathrm{r}(f)$ as the input signal and $N_\mathrm{b}(f)$ as the output signal:

$$H_\mathrm{lr}(f) = \frac{k_+ N_r}{k_- + j2\pi f}. \tag{2.17}$$

The transfer function of the LR binding process corresponds to that of a low-pass filter, characterized by a cutoff frequency of $f_\mathrm{c,lr} = k_-/2\pi$. Utilizing (2.17), the spectral density of the output signal, i.e., time-varying number of bound receptors, can be obtained as follows:

$$N_\mathrm{b}(f) = H_\mathrm{lr}(f)\Phi_\mathrm{r}(f) = \frac{k_+ N_r}{k_- + j2\pi f}\Phi_\mathrm{r}(f). \tag{2.18}$$

The normalized gain for the LR binding process is

$$\Gamma_\mathrm{lr}(f) = \frac{|H_\mathrm{lr}(f)|}{\max_\mathrm{f}(|H_\mathrm{lr}(f)|)} = \frac{k_-}{\sqrt{4\pi^2 f^2 + k_-^2}}. \tag{2.19}$$

The delay for the LR binding process $\tau_{\mathrm{lr}}(f)$ is

$$\tau_{\mathrm{lr}}(f) = -\frac{d\varphi_{\mathrm{lr}}(f)}{df} = \frac{2\pi}{k_{-}\left(\left(\frac{2\pi f}{k_{-}}\right)^{2} + 1\right)}, \tag{2.20}$$

where $\varphi_{\mathrm{lr}}(f)$ is the phase of $H_{\mathrm{lr}}(f)$ is derived as

$$\varphi_{\mathrm{lr}}(f) = \arctan\left(\frac{\mathrm{Im}(H_{\mathrm{lr}}(f))}{\mathrm{Re}(H_{\mathrm{lr}}(f))}\right) = -\arctan\left(\frac{2\pi f}{k_{-}}\right). \tag{2.21}$$

2.2.3 Transfer Function of Graphene BioFET-based MC Receiver

We consider a graphene bioFET-based MC receiver fabricated on a Si/SiO_2 substrate with a monolayer graphene, which is connected to power sources via deposited metal (Cr/Au) drain and source contacts insulated from the electrolyte MC channel through an insulator layer (e.g., thin Al_2O_3 film), as shown in Fig. 2.2(a). A bio-recognition layer is incorporated onto the surface of graphene, comprising receptors that interact with ligands through the LR binding process. A DC potential, denoted as V_{ref}, is applied to the electrolyte to determine the operating point. This receiver architecture has been previously implemented by our group and its fabrication methodology was detailed in [Kuscu et al., 2021]. In this architecture, binding of charged ligands to the receptors attached uniformly to the graphene surface results in the modulation of the charge carrier density of the transducer channel, i.e., graphene, through electric field effect. This change in charge carrier density modulates the conductance of the channel, and hence the drain-to-source current (ΔI_{ds}) of the receiver. Therefore, the alteration in ΔI_{ds} under constant drain-to-source bias (V_{ds}) becomes a function of the number of bound ligands (which is equal to the number of bound receptors $N_{\mathrm{b}}(t)$) and the electrical charge of the bound ligands. Therefore, the bound ligands can be considered functionally equivalent to the gate of the transistor.

In conventional FETs, the effect of gate potential on ΔI_{ds} is quantified through the transconductance of the transistor, denoted by G_{m}. Likewise, the impact of ligands bound to receptors on ΔI_{ds} can be measured through transconductance. Therefore, transconductance plays a vital role in shaping the input-output relation-

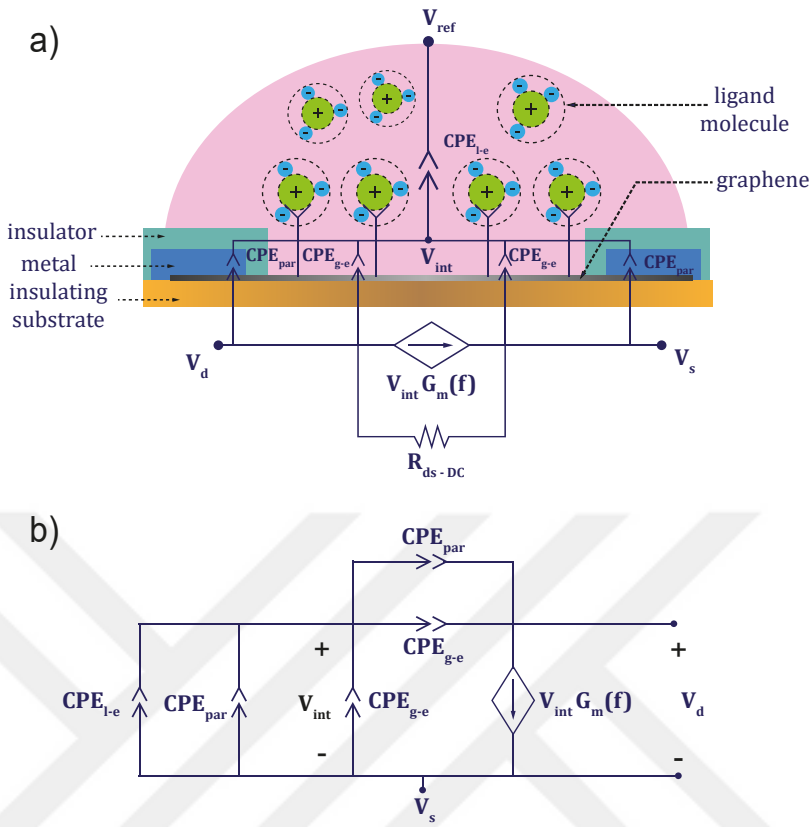

Figure 2.2: (a) Schematic of the graphene bioFET combined with the equivalent circuit. (b) Small-signal equivalent model of the graphene bioFET.

ship of the MC receiver, and the frequency-domain representation of the transconductance, denoted as $G_{\mathrm{m}}(f)$, becomes a key part of the transfer function of the MC receiver, referred to as $H_{\mathrm{t}}(f)$. Nevertheless, there is an additional component that contributes to $H_{\mathrm{t}}(f)$, which will be further explained.

To obtain the $G_{\mathrm{m}}(f)$, we can use a small-signal model, which is an AC equivalent circuit that approximates the nonlinear behavior of the device with linear elements. In this study, we build on the small-signal model developed in [Garcia-Cortadella et al., 2020] for graphene solution-gated FETs, used as a neural interface, to obtain the input-output relation in frequency-domain with the input being the time-varying number of bound receptors and the output being the drain-to-source current. Fig. 2.2(a) presents the schematic of the MC receiver combined with the equivalent circuit to depict physical origin of each element, and Fig. 2.2(b) demonstrates the small-

signal model of the MC receiver.

We start modeling the MC receiver by investigating solid-liquid interface behavior. The interface of a charged surface and an electrolyte is commonly referred to as an electrical double layer (EDL) [Stojek, 2010]. The electrons on the charged surface and the ions on the electrolyte are separated by a single layer of solvent molecules that stick to the charged surface and act as a dielectric in a conventional capacitor. Hence, EDL properties are generally modeled as a capacitor in the literature [Khademi and Barz, 2020]. In this model, however, the graphene-electrolyte interface is described as a constant phase element (CPE) (i.e., CPE_{g-e}) rather than an ideal capacitor to precisely characterize the response of the EDL in graphene bioFETs. The CPE behavior of the graphene-electrolyte interface stems from the presence of charged impurities on the substrate and structural imperfections within the graphene lattice, potentially resulting in a non-uniform local density of states (DOS) [Sun and Liu, 2019].

The impedance of a CPE can be written as follows [Barsoukov and Macdonald, 2005]:

$$Z = \frac{1}{Q_0(j2\pi f)^{\alpha}}, \tag{2.22}$$

where Q_0 is the admittance at $f = 1/2\pi$ Hz and α is a parameter that determines the phase angle. The values of both Q_0 and α depend on the applied voltage (which results from the bound charged ligands) and reflect the properties of the graphene-electrolyte interface. A CPE with $\alpha = 1$ behaves like an ideal capacitor, while a CPE with $\alpha = 0$ behaves like a pure resistor. A CPE with $0 < \alpha < 1$ represents an imperfect capacitor that has a non-constant capacitance value. The capacitance of a CPE (i.e., C_{CPE}) can be calculated by equating the imaginary part of the impedance of CPE to the impedance of an ideal capacitor, as proposed by Hsu et al. [Hsu and Mansfeld, 2001]. This approach yields the following expression for the capacitance of a CPE:

$$C_{CPE} = \frac{Q_0}{(2\pi f)^{1-\alpha}} \exp\left(j\frac{\pi}{2}(\alpha - 1)\right). \tag{2.23}$$

The bio-recognition layer can be modeled as a charged capacitor according to Xu et al. [Xu et al., 2017]. This represents the double-layer capacitance between a single

ligand and electrolyte. In this model, the ligand-electrolyte interface is described as a CPE, which is denoted as CPE_{l-e}, with $\alpha = 1$ to mimic the behavior of an ideal capacitor and ensure notational consistency within the overall model. When charged ligands bind to receptors, they generate a small signal variation in the gate potential. This variation is transduced into a voltage at the graphene-electrolyte interface (V_{int}). A current source element $V_{\text{int}}G_{\text{m}}(f)$ is used to model the conversion of AC signals at the gate into AC signals in the drain current (I_{ds}), where $G_{\text{m}}(f)$ is the transconductance of the bioFET. To account for the DC current flowing through the graphene bioFET caused by the reference voltage (V_{ref}), a resistive element R_{ds-DC} is employed in the model. However, during small signal analysis, when V_{ref} is set to zero, the R_{ds-DC} is removed from the small signal model depicted in Fig 2.2(b). To account for parasitic capacitances in the device that arise as a result of the coupling between electrolyte and the contact metals through the insulating layer, another CPE, CPE_{par}, is included in parallel with CPE_{g-e}. As it will be revealed, this CPE affects the high-frequency response of the bioFET. Using this equivalent circuit, we can obtain the frequency-domain representation of transconductance as follows [Garcia-Cortadella et al., 2020]:

$$G_{\text{m}}(f) = \left.\frac{dI_{ds}}{dV_{int}}\right|_{v_{ds}} + G_{\text{m,eff}}. \tag{2.24}$$

The derivative term on the RHS of (2.24) represents the intrinsic transconductance, which is the change in the drain current with respect to the interface potential. The intrinsic transconductance depends on the interface capacitance between the graphene and the electrolyte (CPE_{g-e}), which reflects the charge accumulation at the interface. This relationship is given by

$$\left.\frac{dI_{ds}}{dV_{int}}\right|_{v_{ds}} = V_{ds}\frac{w_g}{l_g}\mu_g C_{CPE_{g-e}}, \tag{2.25}$$

where w_g and l_g represent the width and length of the graphene transduction channel, respectively, and μ_g denotes the charge carrier mobility of graphene [Xu et al., 2011]. The interface capacitance (i.e., $C_{CPE_{g-e}}$) can be obtained using (2.23) to have a frequency-dependent relation for the intrinsic transconductance.

An additional term, $G_{m,eff}$, contributes positively to the gain of the transduction process at high frequencies. The interface capacitances $C_{CPE_{g-e}}$ and $C_{CPE_{par}}$ lead

to a direct capacitive current between the gate and the graphene bioFET contacts, which is evenly distributed to the drain and source. This contribution, independent of field-effect coupling, can be regarded as an effective transconductance term. As shown in Fig. 2.3, which plots the magnitude of $|G_m(f)|$ over a range of frequencies for MC receiver, the capacitive contribution to the drain current dominates the frequency response beyond a certain frequency threshold. This contribution can be expressed as [Garcia-Cortadella et al., 2020]:

$$G_{\mathrm{m,eff}}(f) = 1/(2Z_{CPE_{g-e}}) + 1/(2Z_{CPE_{par}}). \tag{2.26}$$

By explicitly incorporating the frequency dependence in (2.22) for (2.26), the second term in (2.24) can be derived as follows:

$$G_{\mathrm{m,eff}}(f) = Q_{g-e}(2\pi f)^{\alpha_{g-e}} e^{j\frac{\pi}{2}\alpha_{g-e}} + Q_{par}(2\pi f)^{\alpha_{par}} e^{j\frac{\pi}{2}\alpha_{par}}. \tag{2.27}$$

By combining (2.24) with (2.25), and (2.27), the frequency-dependent transconductance of a MC receiver can be expressed as:

$$G_{\mathrm{m}}(f) = \pm V_{ds}\frac{w_g}{l_g}\mu_g\frac{Q_{g-e}}{(2\pi f)^{1-\alpha}}e^{j\frac{\pi}{2}(\alpha_{g-e}-1)} + Q_{g-e}(2\pi f)^{\alpha_{g-e}}e^{j\frac{\pi}{2}\alpha_{g-e}} + Q_{par}(2\pi f)^{\alpha_{par}}e^{j\frac{\pi}{2}\alpha_{par}}. \tag{2.28}$$

The equation above uses the $\pm$ sign, which is positive in the electron conduction regime, and negative in the hole conduction regime of the bioFET. In this study, we focused on the hole conduction regime when plotting $|G_{\mathrm{m}}(f)|$ and conducting the simulations. In Fig. 2.3, two distinct response regimes can be identified: (i) a *CPE dominant* regime (up to 1 kHz), and (ii) a Z_{CPE} *current* regime where G_{m} increases due to capacitive currents (above 1 kHz).

To obtain the transfer function of the bioFET-based MC receiver, i.e., $H_{\mathrm{t}}(f)$, in addition to $G_{\mathrm{m}}(f)$, we need to derive the potential created by a single ligand on the graphene surface (V_{int}). As it will be revealed, by including $V_{\mathrm{int}}(f)$ in the $H_{\mathrm{t}}(f)$, we will be able to derive the spectral density of the output current, i.e., $I_{\mathrm{m}}(f)$, through end-to-end transfer function. The effective charge on the graphene surface resulting from binding of each ligand to the receptor is determined by the

expression $Q_{\mathrm{m}} = q_{\mathrm{eff}} N_{e^-}$, where N_{e^-} denotes the average number of free electrons per ligand. The mean effective charge, q_{eff}, represents the charge that a single electron of a ligand can generate on the graphene surface in the presence of ionic screening in the medium. The relationship is given by $q_{\mathrm{eff}} = q \times \exp(-r/\lambda_{\mathrm{D}})$ where q is the elementary charge and r represents the average distance between the ligand electrons in the bound state and the surface of the transducer. It is assumed that this average distance is equivalent to the average length of the surface receptor in the bound state [Kuscu and Akan, 2016a]. The Debye length, λ_{D}, characterizes the ionic strength of the medium, and is given by

$$\lambda_{\mathrm{D}} = \sqrt{(\epsilon_M k_B T)/(2 N_A q^2 c_{ion})}, \tag{2.29}$$

where ϵ_M is the dielectric permittivity of the medium, k_B is Boltzmann's constant, T is the temperature, N_A is Avogadro's number, and c_{ion} is the ionic concentration of the medium [Rajan et al., 2013]. Finally, the interface potential generated by the charge accumulated on the surface by a single ligand is as follows [Kuscu and Akan, 2016a]:

$$V_{\mathrm{int}}(f) = \frac{Q_{\mathrm{m}}}{C_{CPE_{eq}}}, \tag{2.30}$$

where $C_{CPE_{eq}}$ is the equivalent capacitance of the transducer, which is comprised of a parallel combination of CPE_{l-e}, CPE_{g-e}, and CPE_{par} connected in series with another parallel pair of CPE_{g-e} and CPE_{par} as shown in Fig. 2.2(b). This can be expressed as:

$$C_{CPE_{eq}} = \left(\frac{1}{C_{CPE_{l-e}} + C_{CPE_{g-e}} + C_{CPE_{par}}} + \frac{1}{C_{CPE_{g-e}} + C_{CPE_{par}}} \right)^{-1}, \tag{2.31}$$

where frequency-dependent relation of all C_{CPE} terms can be obtained by utilizing (2.23). Therefore, the transfer function of the transduction process in a graphene bioFET-based MC receiver, i.e., $H_{\mathrm{t}}(f)$, can be written by using (2.24) and (2.30) as

$$H_{\mathrm{t}}(f) = V_{\mathrm{int}}(f) G_{\mathrm{m}}(f). \tag{2.32}$$

The normalized gain of the transduction process can be numerically computed using (2.32) as

$$\Gamma_{\mathrm{t}}(f) = \frac{|H_{\mathrm{t}}(f)|}{\max_{\mathrm{f}}(|H_{\mathrm{t}}(f)|)}. \tag{2.33}$$

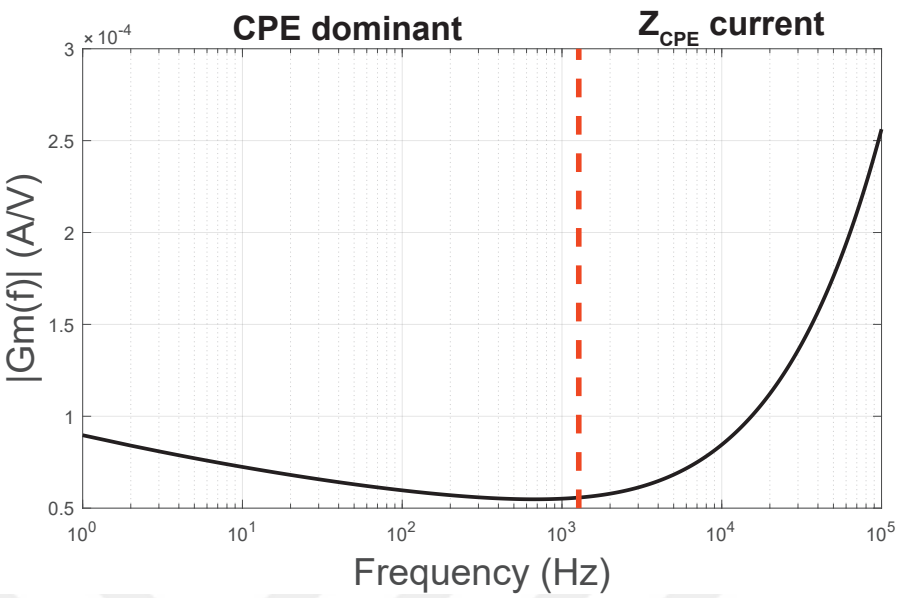

Figure 2.3: Transfer function ($G_m(f)$) of graphene bioFET composed of two different response regime: (i) CPE-dominant regime and (ii) Z_{CPE} current regime.

The delay of the transduction process is as $\tau_{\mathrm{t}}(f)$ is

$$\tau_{\mathrm{t}}(f) = -\frac{d\varphi_{\mathrm{t}}(f)}{df}, \tag{2.34}$$

where $\varphi_{\mathrm{t}}(f)$ is the phase of $H_{\mathrm{t}}(f)$ is derived as

$$\varphi_{\mathrm{t}}(f) = \arctan\left(\frac{\mathrm{Im}(H_{\mathrm{t}}(f))}{\mathrm{Re}(H_{\mathrm{t}}(f))}\right). \tag{2.35}$$

2.2.4 End-to-End Transfer Function and Output Current Spectrum

The end-to-end transfer function of a microfluidic MC channel with graphene bioFET-based receiver can be expressed using Equations (2.6), (2.17), and (2.32) as follows

$$\begin{aligned} H(f) &= H_{\mathrm{p}}(f) \times H_{\mathrm{lr}}(f) \times H_{\mathrm{t}}(f) \\ &= V_{\mathrm{int}}(f) G_{\mathrm{m}}(f) \left(\frac{k_+ N_r}{k_- + j2\pi f}\right) e^{-\left(\frac{(2\pi f)^2 D}{u^3} + j\frac{2\pi f}{u}\right) x_r}. \end{aligned} \tag{2.36}$$

Spectral density of the output current can be obtained by using the end-to-end transfer function and the spectral density of the input concentration signal as:

$$I_{\mathrm{m}}(f) = H(f) \times \Phi_{\mathrm{in}}(f). \tag{2.37}$$

The end-to-end normalized gain is calculated by multiplying the individual contributions of normalized gain from each module across the frequency spectrum f as

$$\Gamma(f) = \Gamma_{\mathrm{p}}(f) \times \Gamma_{\mathrm{lr}}(f) \times \Gamma_{\mathrm{t}}(f). \tag{2.38}$$

The end-to-end delay is determined by summing the delay contributions from each module across the frequency spectrum f as follows:

$$\tau(f) = \tau_{\mathrm{p}}(f) + \tau_{\mathrm{lr}}(f) + \tau_{\mathrm{t}}(f). \tag{2.39}$$

2.3 Numerical Results

In this section, we present the numerical results obtained using the developed analytical frequency-domain model, which is validated through particle-based simulations under various settings. The default values for the parameters used in the analyses are provided in Table 2.1. Throughout the simulations, we employed the default values listed in Table 2.1 for system parameters. We altered one parameter at a time to evaluate its impact on our model's behavior. This approach allowed us to illustrate the boundaries within which our model performs effectively, taking into account the assumptions made during the derivation of the transfer function for ligand propagation and LR interaction. The admittance and phase angle values for CPE_{g-e} and CPE_{par} are extracted from the experimentally fitted data in [Garcia-Cortadella et al., 2020], conducted in an electrolyte medium with an ionic strength of 0.5 mM. We considered the same ionic strength ($c_{ion} = 0.5$ mM). As for the admittance of CPE_{l-e}, it is assigned considering the fact that the area of the double-layer interface between ligands and electrolyte is significantly smaller compared to the double-layer surface at the graphene-electrolyte interface. Consequently, based on the parallel plate capacitor formula $C = \varepsilon \frac{A}{d}$, where ε is permittivity, and d is the distance between the surface layers (a single layer of molecules in this case), it is evident that the capacitive behavior of CPE_{l-e} are significantly lower compared to CPE_{g-e} since the values of A and d remain the same for both interfaces. We set $\mu_g = 200$ cm^2/Vs as reported in [Kuscu et al., 2021]. Aptamers are utilized as the receptors, and their

default length is defined as 2 nm [Kuscu and Akan, 2016b]. Binding and unbinding rates, k_+ and k_- are set considering the assumption of (2.15) and accepted values in the MC literature [Pierobon and Akyildiz, 2011b]. We consider the microfluidic channel with a cross-sectional height of $h_{ch} = 3$ μm, a width of $w_{ch} = 3$ μm, and a length of $l_{ch} = 200$ μm, resulting in a laminar and steady flow. The simulations were performed using *Smoldyn*, a particle-based spatial stochastic simulation framework that offers high spatiotemporal resolution by simulating each molecule of interest individually [Andrews, 2017]. This approach captures the inherent stochasticity of molecular transport and reactions and provides nanometer-scale spatial resolution.

The simulation setup consisted of a straight microfluidic channel with a rectangular cross-section, as shown in Fig. 2.4. The receptor molecules were immobilized at the channel bed, representing the 2d MC receiver. An input rectangular pulse signal composed of ligands was introduced at the inlet of the channel as shown in Fig. 2.4(a). These ligands propagated towards the receptors through convection and diffusion as depicted in Fig. 2.4(b). A fraction of the ligands randomly bound to the receptor molecules for varying durations, depending on their kinetic interaction rates. Subsequently, they unbound and continued their propagation until they exited the channel at the outlet, as demonstrated in Fig. 2.4(c).

The particle-based spatial stochastic simulation also accounts for various noise sources in the emission, propagation, and reception processes. These included particle sampling noise, which emerges during the emission process, modulating the concentration rate of particles due to the discrete nature of ligands forming the pulse concentration; particle counting noise, related to the random nature of the diffusion process during ligand propagation, leading to unwanted perturbations in the received concentration; and ligand-receptor binding noise, characterized by random fluctuations in the LR binding process [Pierobon and Akyildiz, 2011b, Pierobon and Akyildiz, 2011a]. These noise factors were not considered in our deterministic model, which assumed a large number of ligands in each transmission cycle, making the concentration perturbation negligible. This assumption has been substantiated through a thorough comparison of our deterministic model with stochastic simulation. To validate the model in both time and frequency domains, we evaluated

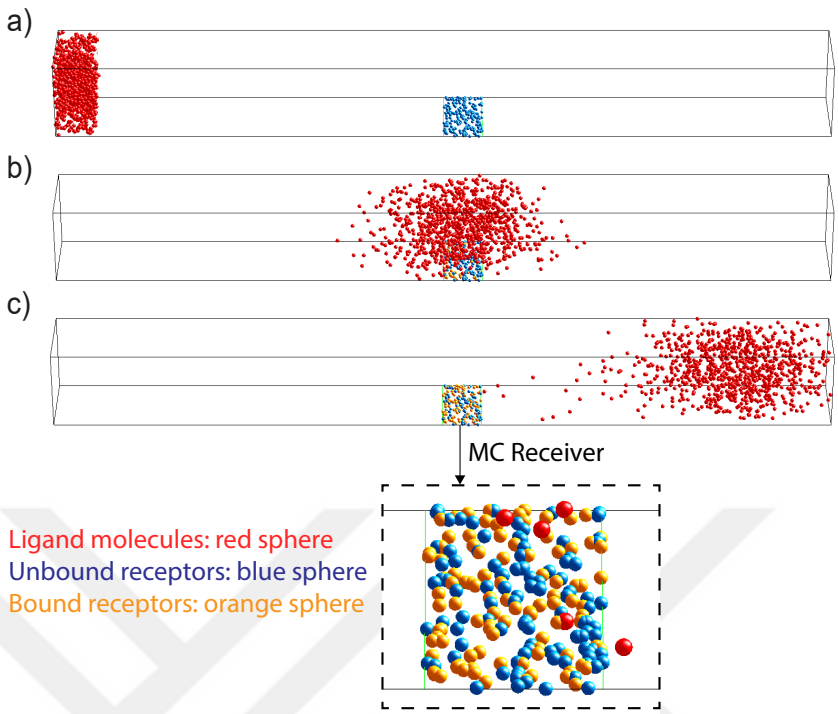

Figure 2.4: Smoldyn simulation environment: (a) A pulse concentration of ligands is released into the microfluidics MC channel. (b) The pulse around the MC receiver position, where ligands initiate interactions with receptors. The dispersion of the pulse signal occurs as a result of ligand diffusion. (c) Pulse signal approaches the channel end leaving behind ligands bound to receptors.

the transfer function of the propagation channel, the transfer function of the LR binding process, and the end-to-end frequency-domain model under varying system parameters. This evaluation was conducted using both analytical expressions and simulation results. The particle-based simulation does not incorporate the transfer function of the MC receiver. Therefore, the numerical results for $H_{\mathrm{t}}(f)$ are solely obtained using analytical expressions. As the transduction process cannot be simulated through particle-based approach, the end-to-end results for output current spectral density in Section 2.2 are obtained solely using the analytical expressions we derived in Section 2.2.4. Moreover, we calculated the sampling frequency utilizing a numerical method for varying system parameters.

Table 2.1: Default Values of Simulation Parameters

Admittance for CPE_{g-e} (Q_{g-e})	1.6 μFs$^{\alpha-1}$/cm^2
Constant angle of impedance for $CPE_{g-e}(\alpha_{g-e})$	0.905
Admittance for CPE_{par} (Q_{par})	8 nFs$^{\alpha-1}$
Constant angle of impedance for CPE_{par} (α_{par})	0.6
Admittance for CPE_{l-e} (Q_{l-e})	5.4 fFs$^{\alpha-1}$
Constant angle of impedance for CPE_{l-e} (α_{l-e})	1
Graphene channel width (w_g)	1 μm
Graphene channel length (l_g)	3 μm
Drain to source voltage (V_{ds})	0.1 V
Mobility of graphene (μ_g)	2×10^3 cm^2/Vs
Ionic strength of electrolyte medium (c_{ion})	0.5 mM
Relative permitivity of medium (ϵ_M/ϵ_0)	80
Temperature (T)	300 K
Length of a surface receptor (r)	2 nm
Diffusion coefficient of ligands (D)	10 $^{-11}$ m^2/s
Microfluidic channel height (h_{ch})	3 μm
Microfluidic channel width (w_{ch})	3 μm
Microfluidic channel length (l_{ch})	200 μm
Transmitter-receiver distance (x_r)	100 μm
Flow velocity (u)	2×10^{-3} m/s
Binding rate (k_+)	10^{-18} m^3/s
Unbinding rate (k_-)	500 s^{-1}
Pulse concentration (C_m)	3.3×10^{20} m^{-3}
Average number of electrons in a ligand (N_{e^-})	3
Number of receptors on the sensor surface (N_r)	500
Pulse width (T_p)	0.5 ms
Simulation time step (Δt)	50 μs

2.3.1 Propagation Channel

Effect of Varying Pulse Width

The first analysis investigates the impact of varying pulse width, T_p, a critical parameter commonly employed in signal generation and modulation schemes, such as pulse width modulation (PWM) [Garrison et al., 2018]. The results of this analysis are presented in Fig. 2.5. As expected, an increase in pulse width leads to a higher concentration value in time domain, as shown in Fig. 2.5(a). In the frequency domain (Fig. 2.5(b)), a higher amplitude is observed in the spectral density of the

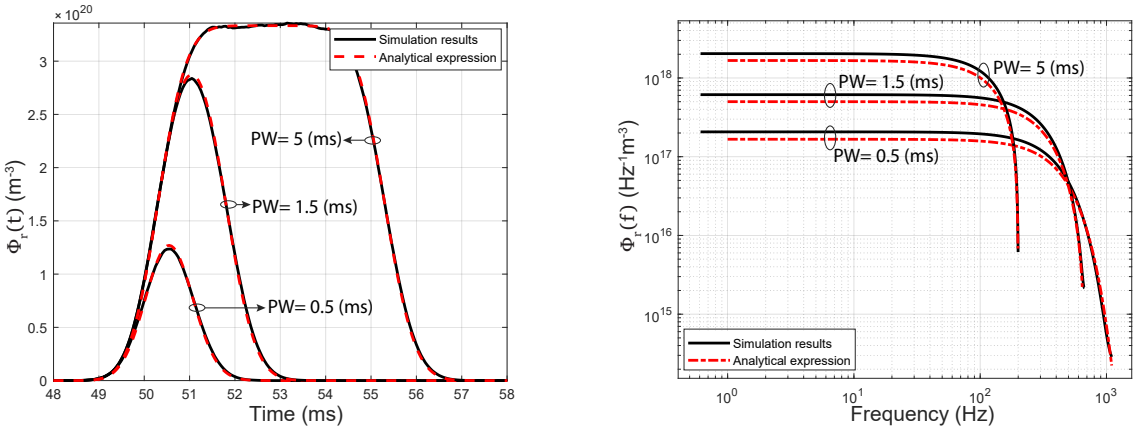

(a) **(b)**

Figure 2.5: (a) The analytical and simulation results of time-domain channel response under varying pulse width. (b) Spectrum pulse concentrations signal with varying pulse width driven from analytical model and simulation results.

received concentration, $\Phi_{\mathrm{r}}(f)$, as the pulse width increases. Moreover, the cutoff frequency decreases with the increasing pulse width, which is consistent with the expectations based on Equations (2.4) and (2.9). The analytical model exhibits a high degree of agreement with the simulation results. It is important to note that as pulse width increases, the likelihood of inter-symbol interference also rises, leading to potential challenges in the signal recovery process.

Effect of Varying Diffusion Coefficient

We also analyze the impact of varying diffusion coefficient of ligands, D, on the response of the MC system. The diffusion coefficient is a fundamental parameter in MC systems, as it determines the rate at which molecules disperse through the medium. Additionally, it introduces particle counting noise to the MC system. Molecules with a higher diffusion coefficient disperse more, resulting in a broader received signal width. Additionally, the peak received concentration decreases due to the higher dispersion, as shown in Fig. 2.6(a). On the other hand, in the frequency domain, increasing the diffusion coefficient is reflected in a slight decrease in the

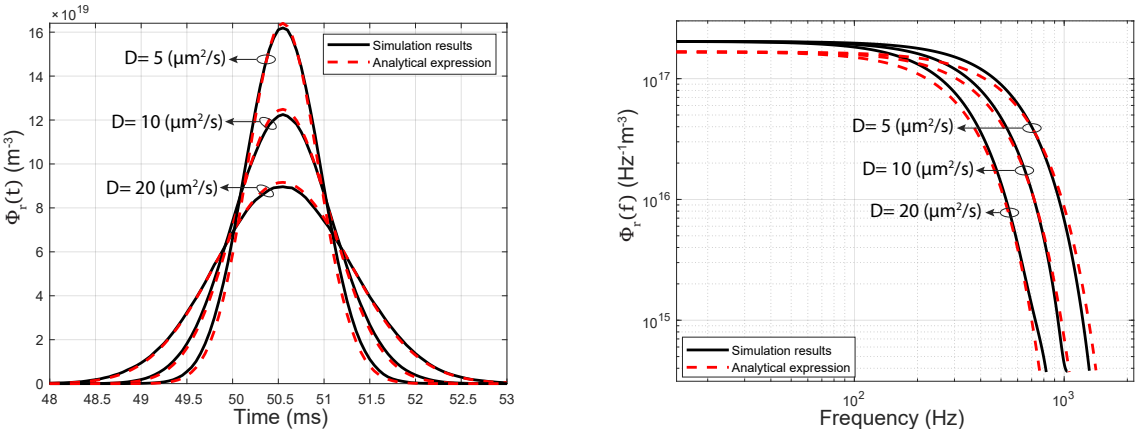

(a) **(b)**

Figure 2.6: (a) Concentration of pulse signals with varying diffusion coefficient in time domain. (b) Spectrum of pulse concentration in a varying diffusion coefficient setting.

cutoff frequency of the spectral density of the received concentration, $\Phi_{\mathrm{r}}(f)$, for both analytical and simulation results, as demonstrated in Fig. 2.6(b).

2.3.2 Ligand-Receptor Binding Process

Effect of Varying Binding Rate

We investigate the effect of varying binding rates, k_+, on the time-varying number of bound receptors in both time and frequency domains. Fig. 2.7(a) demonstrates that an increase in the binding rate directly corresponds to an increased number of bound receptors, $N_{\mathrm{b}}(t)$, as molecules with higher binding rate exhibit a higher propensity to bind to the receptors when they are in close proximity of each other. Similarly, as expected from Equation (2.18), the frequency domain analysis reveals a higher amplitude in the spectral density of the number of bound receptors, $N_{\mathrm{b}}(f)$, when binding rates are increased, as shown in Fig. 2.7(b).

Effect of Varying Unbinding Rate

We also investigate the impact of varying unbinding rates, k_-, on the number of bound receptors. Contrary to the effect of binding rates, increasing the unbinding

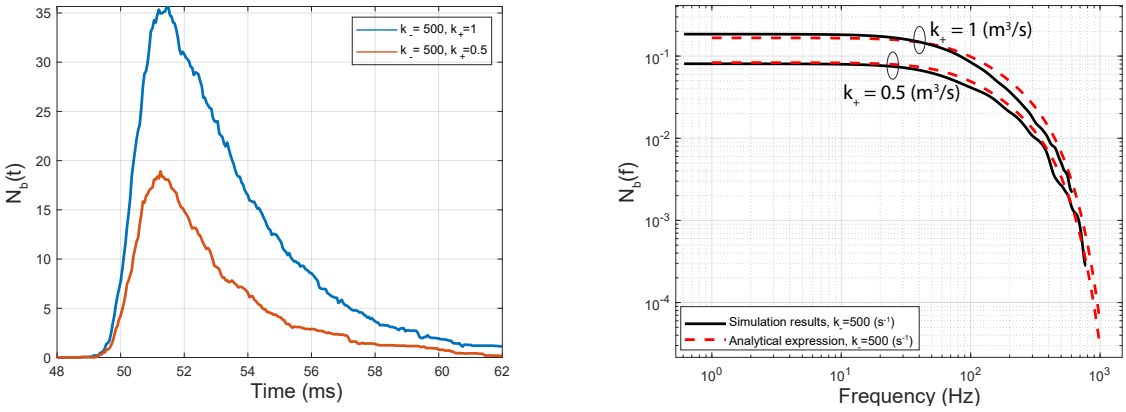

(a) **(b)**

Figure 2.7: (a) Number of bound receptors for varying binding rate in time-domain. (b) Spectrum of number of bound receptors for varying binding rate

rate leads to a decrease in the number of bound receptors in the time-domain, $N_{\mathrm{b}}(t)$, as shown in 2.8(a). Molecules with higher unbinding rate have shorter bound state durations. In the frequency domain, as shown in Fig. 2.8(b), the unbinding rate exhibits an inverse relationship with the spectral density, as described by (2.18). Consequently, a higher unbinding rate results in a lower amplitude in the spectral density of bound receptors, $N_{\mathrm{b}}(f)$, a finding supported by both simulation and analytical results.

2.3.3 End-to-End Model

Effect of Varying Pulse Width

To evaluate the end-to-end model's accuracy and investigate the impact of varying pulse widths, T_p, we analyze the spectral density of output current, $I_{\mathrm{m}}(f)$, for three pulse signals with different pulse widths but identical amplitudes, i.e., concentrations, as shown in Fig. 2.9(a). As predicted in Section 2.3.1, an increase in pulse width corresponds to a higher amplitude in $I_{\mathrm{m}}(f)$. This phenomenon occurs because a wider ligand pulse results in a higher concentration of ligands in the vicinity of the receiver's receptors. This, in turn, increases the probability of binding to a

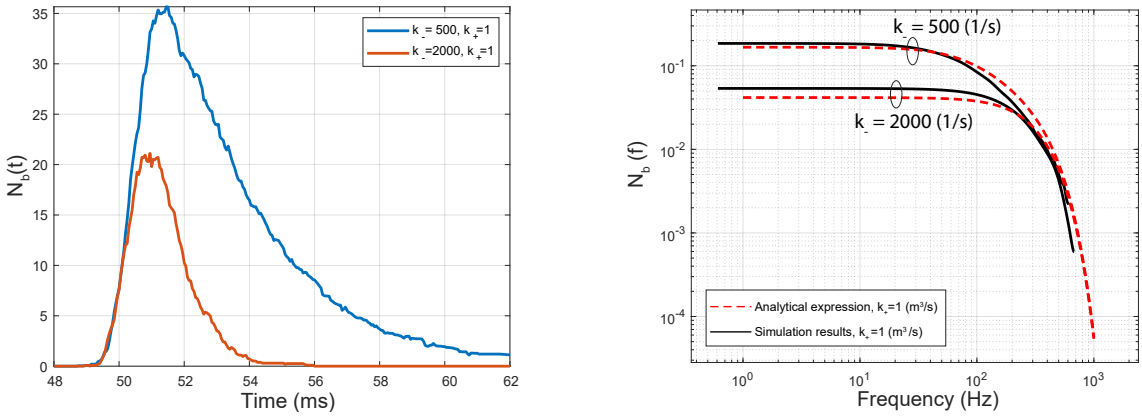

(a) **(b)**

Figure 2.8: (a) Number of bound receptors for varying unbinding rate in time-domain. (b) Spectrum of the number of bound receptors for varying unbinding rate.

receptor before the already bound ones dissociate, resulting in a higher number of observed bound receptors, i.e., amplitude. The analytical expression for the output current spectrum, represented by (2.37) and incorporating the transfer function of the three main processes and the input signal concentration, demonstrates high accuracy when compared to the simulation results.

Effect of Varying Ligand Concentration

We also evaluate the impact of varying ligand concentrations, C_m, on the end-to-end model by performing simulations with input concentration pulses with different concentrations but identical pulse widths. By analyzing the spectral density of the resulting output current, $I_{\mathrm{m}}(f)$, we observe that the amplitude of $I_{\mathrm{m}}(f)$ increases as concentration increases, as depicted in Fig. 2.9(b). The simulation results are strongly aligned with the analytical results obtained from (2.37).

2.3.4 End-to-End Gain and Delay

The propagation of input signals, LR interaction, and transduction processes introduce both gain and delay to the communication system. In this section, we illustrate the end-to-end gain and delay and examine the influence of each component on them

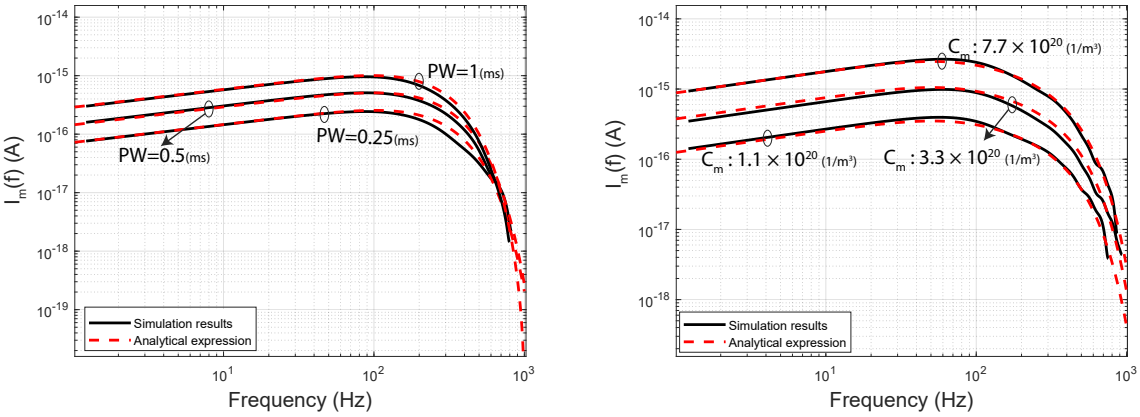

(a) **(b)**

Figure 2.9: Spectrum of output current (end-to-end model) from analytical expression and simulation results (a) for varying pulse width PW, (b) for varying amplitude of input concentration pulse C_m.

in the MC system. According to (2.10) and (2.19), we expect a decline in gain as the frequency increases in both propagation and LR interaction processes. The attenuation in propagation is attributed to signal diffusion, reducing peak concentration during propagation. Similarly, in the LR process, attenuation occurs because only a small portion of received ligands interacts with the receptor, further diminishing the initial signal. However, in the transduction process, the signal experiences amplification, owing to the amplifying characteristics of the field-effect transistor. As can be seen in Fig. 2.10(a), the end-to-end gain, encompassing the combination of gains from each module as expressed in (2.38), also exhibits attenuation. The end-to-end delay is illustrated in Fig. 2.10(b), showing a decrease in delay with increasing frequency, as expected. While the delay in the propagation process remains frequency-independent, as obtained in (2.11), the delay in the LR interaction process is found to be inversely proportional to frequency, as derived in (2.20).

2.3.5 Sampling Frequency

To reconstruct the input concentration signal, $\phi_{\text{in}}(t)$, from the sampled sequence of the number of bound receptors, it is essential to employ an appropriate sampling

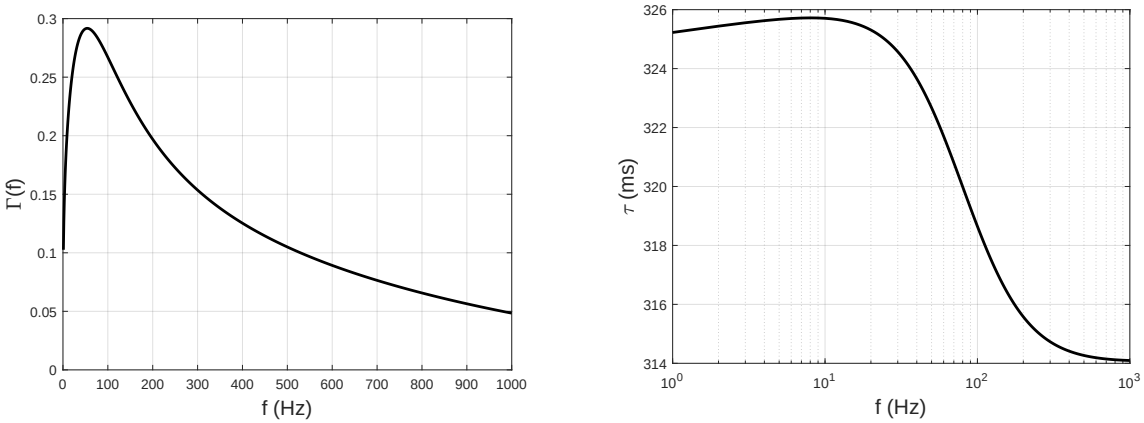

(a) **(b)**

Figure 2.10: (a) The end-to-end gain, $\Gamma(f)$, of MC system calculated using (2.38), and (b) end-to-end delay, $\tau(f)$, of MC system obtained using (2.39).

frequency. Considering that both the input concentration spectral density and the end-to-end transfer function and consequently the resulting output current spectral density, display a Lorentzian-shaped profile, it is essential to determine the cutoff frequency that contains most of the spectrum energy. The energy of the output current spectral density within a bandwidth ranging from 0 Hz to the cutoff frequency can be quantified as follows [Huang et al., 2021b]:

$$\int_0^{f_c} |H(f)\Phi_{\text{in}}(f)|^2 df = \eta \int_0^{+\infty} |H(f)\Phi_{\text{in}}(f)|^2 df, \tag{2.40}$$

where f_c is the cutoff frequency and η is the fraction of the total spectrum energy contained within the interval $(0, f_c)$. In this study, we consider $\eta = 0.99$, which indicates that 99% of the spectral power is contained within the specified bandwidth. Once the cutoff frequency has been determined, the sampling frequency can be obtained using the Nyquist–Shannon theorem, which states that in order to achieve a reconstruction that captures all the information, the sampling frequency should be greater than twice the bandwidth:

$$2f_c \leq f_s \leq \infty. \tag{2.41}$$

Fig. 2.11 shows the sampling frequency obtained from (2.41), which is a function of pulse width T_p, diffusion coefficient D, and flow velocity u. Fig. 2.11(a) demon-

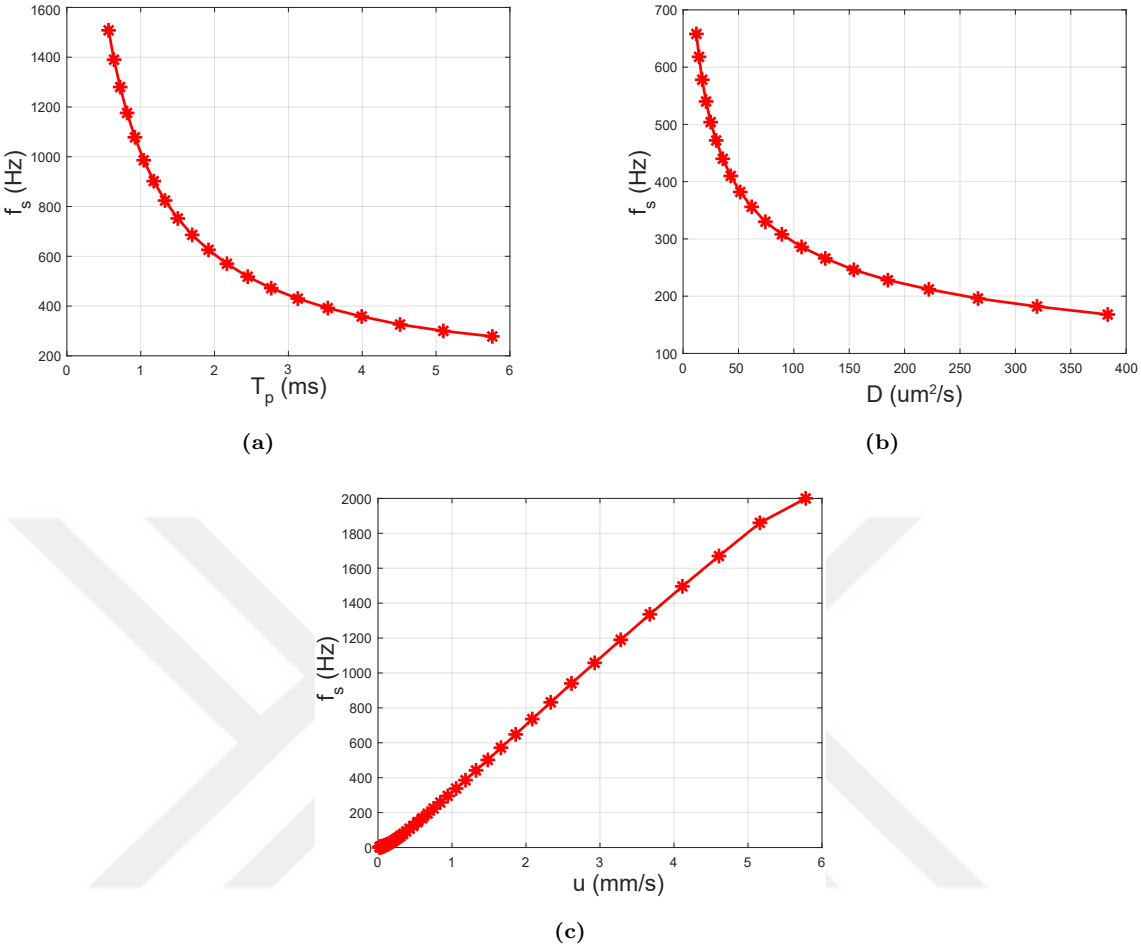

Figure 2.11: Sampling frequency as a function of (a) pulse width, (b) diffusion coefficient, and (c) flow velocity.

strates that increasing the pulse width results in a lower sampling frequency required to reconstruct the original continuous signal. As shown in Fig. 2.5(b), the spectral density of a wider pulse signal has a lower cutoff frequency. Therefore, it is expected that increasing the pulse width would allow a lower sampling frequency.

Fig. 2.11(b) indicates that the sampling frequency decreases as the diffusion coefficient increases. This can be attributed to the reduction in the cutoff frequency while increasing the diffusion coefficient, as shown in Fig. 2.6(b). Therefore, the decrease in sampling frequency aligns with the expectations set by the Nyquist-Shannon theorem.

Finally, Fig. 2.11(c) shows the impact of increasing flow velocity on the sampling

frequency. As the flow velocity increases, the signals traverse the receiver position more quickly, which reduces the time window available for capturing an adequate number of samples from the propagating signal. Consequently, to guarantee the collection of a sufficient number of samples, it is necessary to raise the sampling frequency in response to an increase in flow velocity.

2.4 Conclusion

In this study, we introduced a comprehensive end-to-end frequency-domain model for a practical microfluidic MC system with a graphene bioFET-based receiver. The model provides valuable insights into the dispersion and distortion of received signals, and has the potential to inform the design of new frequency-domain MC techniques, such as modulation and detection, matched filters, and interference-free receiver architectures. The end-to-end transfer function, $H(f)$, incorporates the input-output relationships of three sequential modules: the microfluidic propagation channel, the LR binding process, and the graphene bioFET-based receiver. The accuracy and reliability of the developed model were verified through particle-based spatial stochastic simulations, which demonstrated a high degree of agreement with the analytical expressions.

Chapter 3

GRAPHENE BIOFET-BASED MOLECULAR COMMUNICATION RECEIVER

3.1 Introduction

In this chapter, I present the fabrication and characterization of graphene field-effect transistor-based biosensors (graphene bioFETs), which function as receivers in the molecular communication system as discussed in Chapter 2. This study provides a testbed in relevant dimensions, potentially useful for investigating the biochemical and physical processes affecting the performance of MC systems. Additionally, this receiver is an optimized version of similar work in the literature, offering improvements in sensitivity, detection accuracy, and miniaturization of dimensions.

Graphene is a two-dimensional material composed of a single, one-atom-thick layer of carbon atoms arranged in a honeycomb lattice. Graphene's outstanding mechanical and electronic properties, such as high carrier mobility, high conductivity, and high strength, make it a strong candidate for sensing applications, particularly in a bioFET configuration. Graphene's unique electronic properties stem from its distinctive band structure and the lack of a band gap. Due to these properties and its compatibility with the requirements of MC, such as nanoscale dimensions and flexibility, graphene FETs are a promising candidate for use as MC receivers.

In the remainder of this chapter, I elaborate on the fabrication of a graphene bioFET-based MC receiver and its integration with a microfluidic channel. The device is characterized at each stage of fabrication and functionalization.

3.2 Fabrication of MC Receiver

MC receiver is fabricated using a polycrystalline single-layer graphene (SLG) grown by chemical vapor deposition (CVD), sourced from Graphenea Inc., on an n-type Si/SiO_2 substrate (525 ± 25 μm thick with a 90 nm oxide layer, provided from Nanografi).

The metal contact areas (source, drain, and gate) are defined on the sample using an optical lithography process based on the design shown in Fig. 3.1. Then, 5 nm of Cr and 50 nm of Au were uniformly deposited using electron beam deposition technique with *Kurt J. Lesker Company® Pro Line PVD 200* system at 7.6 $\times 10^{-7}$ Torr. Following the deposition of the contacts, the sample is immersed in acetone to undergo the lift-off process, during which the metals on top of the photoresist layer are removed, leaving behind only the patterned contacts. In the next step, the single-crystal graphene domain was transferred onto the Si/SiO_2 substrate using the wet transfer method, as described in [Kuscu et al., 2021]. The graphene was then patterned into six distinct channels using optical lithography process, followed by dry etching to remove graphene from the unwanted areas through reactive ion etching (RIE) with the *SENTECH ETCHLAB 200* system. During this process, the regions unprotected by photoresist were exposed to O_2 plasma at 10W for 30 seconds under a pressure of 1 Pa, leaving the graphene channels measuring 250 μm in length and 125 μm in width. To prevent parasitic currents between the metal contacts in solution, a 30 nm layer of Al_2O_3 was deposited using atamic layer deposition (ALD) to passivate the contacts. Then, An additional photolithography process was conducted to define the areas for Al_2O_3 etching, including the graphene region, gate electrode, and the outer tips of the Au contacts. A wet etching process was then carried out using phosphoric acid (85% wt. in H_2O, obtained from Sigma-Aldrich) to expose the underlying layers. The fabricated MC receiver is shown in Fig. 3.2(a), with a closer view of the graphene area on the receiver provided in Fig. 3.2(b).

The graphene channels were then integrated with a PDMS microfluidic channel, which was fabricated using a silicon mold through photolithography using SU-8 3050. The microfluidic channel has a width of 10^3 μm and a height of 22 μm. The

PDMS was bonded to the graphene using O_2 plasma, and two 600 μm diameter holes were punctured to serve as the inlets and outlets for the microchannel. The MC receiver integrated with the microfluidic channel is presented in Fig. 3.2(c).

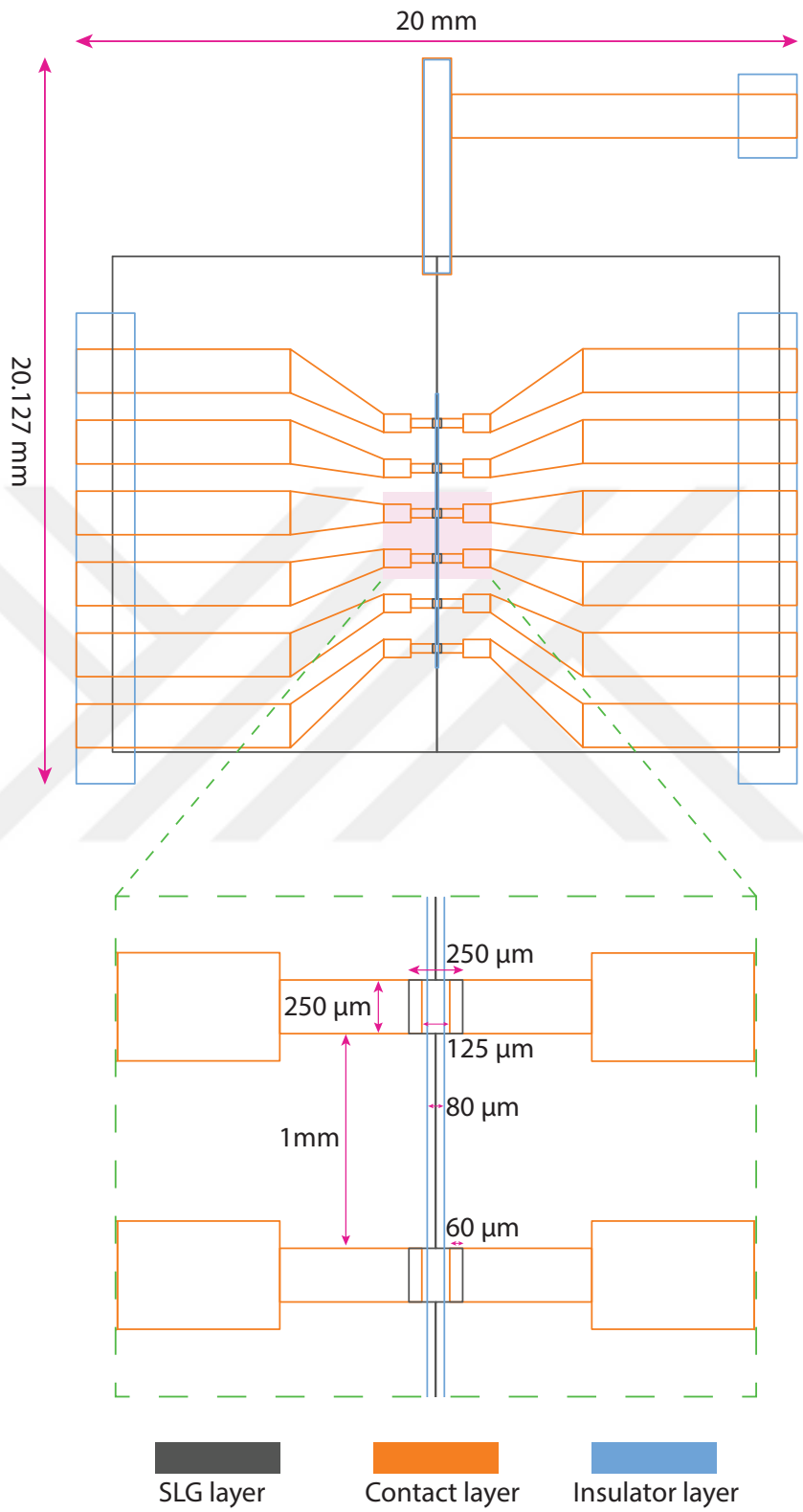

Figure 3.1: Design of MC receiver using computer-aided for optical lithography.

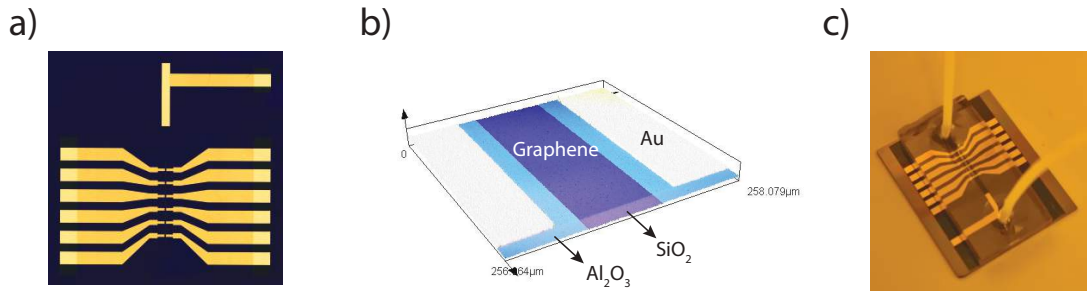

Figure 3.2: a) Optical micrograph of fabricated MC receiver after Al_2O_3 etching process. b) Closer look to area of a graphene channel in MC Receiver. c) MC receiver integrated with PDMS microfulidic channel.

3.3 Ionic Concentration-based Detection

The modulation of graphene's conductance by the applied gate voltage is influenced by the EDL capacitance at the graphene/liquid electrolyte interface, which is affected by the ionic strength of the solution. We explored how ionic concentration impacts graphene conductance. Phosphate buffered saline (PBS, pH 7.4) is used as ionic electrolyte in our experiments. Decreasing PBS concentration results in a positive shift in the Dirac point of the transfer curve, indicating p-type doping.

As outlined in Equation (2.29), the Debye length, λ_D, is inversely proportional to the square root of the solution's ionic strength. Thus, when the ionic concentration increases, λ_D becomes shorter, and the EDL capacitance increases, reducing the V_{GS} needed to accumulate a given amount of charge in the channel. This explains the observed Dirac point shift.

The fabricated graphene bioFET-based MC receivers can be used to decode information based on the concentration of ionic solutions in the medium. Although this approach may decrease the selectivity and specificity of detection due to graphene's high sensitivity to nearby biomolecules, it still offers advantages in terms of ease of implementation and high speed. This is because it eliminates the need for complex functionalization steps, and the sensor's response time to ionic solutions is typically faster than the reaction rate between ligands and receptors. The sensor's response

to varying ionic concentrations is shown in Fig. 3.3. Fig. 3.3(a) shows that as the ionic concentration of the medium decrease from 1xPBS to 0.01xPBS, there is an increase in the drain-source current I_{ds}, indicating a positive shift in the Dirac point of the transfer characteristic. Fig. 3.3(b) illustrates the release of several pulses at three different ionic concentrations (1xPBS, 0.1xPBS, and 0.01xPBS) into the microfluidic channel, showing the sensor's response to these varying concentrations. This method could potentially be used for amplitude modulation in molecular communications. In Fig. 3.3(c), 1xPBS is used as the baseline, and pulses with a short pulse width (60 seconds) in two different concentrations (0.1xPBS and 0.01xPBS) are released into the channel, with the resultant waveforms being recorded. The waveform with the higher amplitude corresponds to 0.01xPBS, while the waveform with the lower amplitude corresponds to 0.1xPBS. It's crucial to note that due to the brief pulse widths, the sensor does not reach equilibrium. However, by analyzing the slope of the rising edge and the peak amplitude reached within 60 seconds, the concentration of the modulated PBS can be determined. This is the key principle of the *pre-equilibrium* detection scheme, which will be discussed in greater detail later in this chapter. This method could greatly enhance detection times and, consequently, data rates, as the time required to reach equilibrium conditions is lengthy, especially for the association and dissociation processes in ligand-receptor interactions.

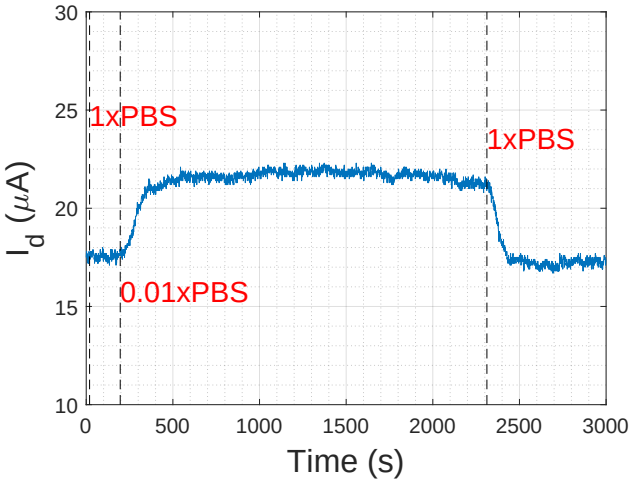

(a)

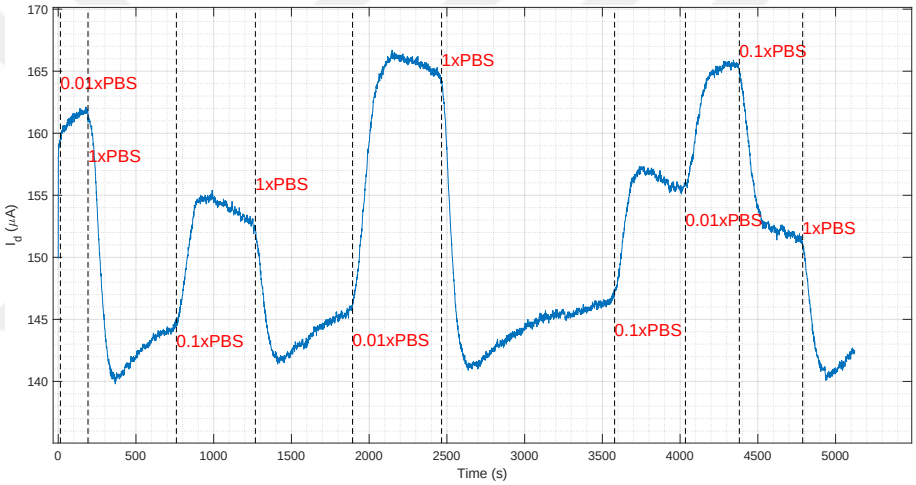

(b)

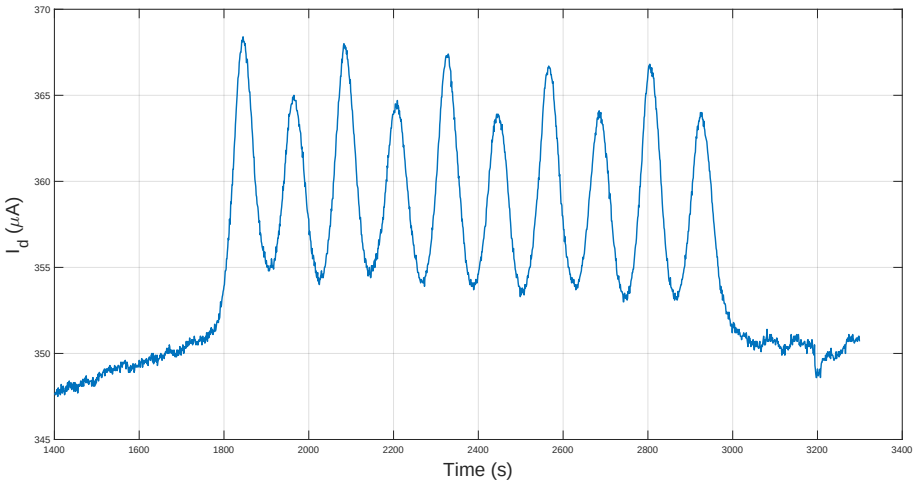

(c)

Figure 3.3: a) Generation of 0.01xPBS pulses over a 1xPBS baseline. b) Pulse generation and detection using 0.1xPBS and 0.01xPBS with 1xPBS as the baseline. c) Waveforms consisting of 0.1xPBS and 0.01xPBS pulses with a constant pulse width of 60 seconds.

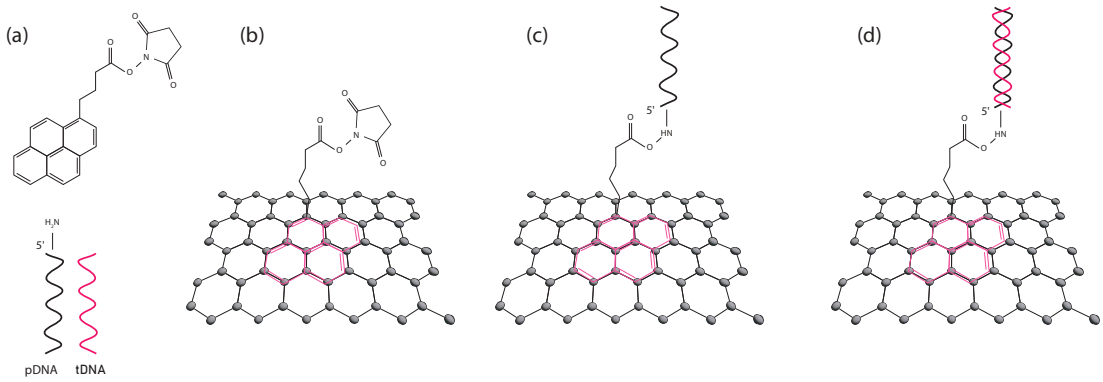

Figure 3.4: a) The molecular structure of PBASE, along with a schematic representation of probe DNA (pDNA) and its matching target DNA (tDNA). b) Noncovalent binding of PBASE to graphene through $\pi - \pi$ interactions. c) The attachment of pDNA through a conjugation process involving the succinimide group of PBASE. d) Hybridization of pDNA and tDNA.

3.4 Functionalisation of GFET

To enhance selectivity and specificity in sensing, as well as to minimize interference from other biochemicals in the sensing environment, it is essential to functionalize the graphene surface with receptors that are selective for the information-carrying molecules. To achieve selectivity, graphene can be bio-functionalized with recognition elements like DNA and antibodies. In this work, since single-stranded DNAs (ssDNAs) are used as target information-carrying molecules (tDNAs), the fabricated GFET is functionalized with probe DNAs (pDNAs) that are complementary to the tDNAs.

To enhance probe DNA immobilization and reduce nonspecific binding, the pristine SLG channels are first functionalized with 1-Pyrenebutyric acid N-hydroxysuccinimide ester (PBASE) linker. This linker contains an aromatic pyrene group that attaches to graphene through $\pi - \pi$ interactions. A 10 mM solution of PBASE in N,N-Dimethylformamide (DMF) is prepared in a glass bottle and sonicated to ensure homogeneous mixing. The prepared PBASE/DMF solution is introduced into the microfluidic channel until the entire channel is filled. The flow is then halted, allowing the SLG channels to be exposed to the PBASE/DMF solution for 2 hours.

After this functionalization step, any unbound PBASE molecules are flushed out with pure DMF, followed by rinsing with PBS.

The next step involves immobilizing 18-mer 5'-amine-modified probe DNAs with the base sequence H2N-(CH2)6-5'-GAG TTG CTA CAG ACC TTC GT-3'. These DNAs, custom-designed and obtained from Sigma Aldrich, are prepared as a 2 µM solution in PBS. This solution is introduced into the microfluidic channel and flowed over the SLG channels. Once the channel is filled with the pDNAs solution, the inlet and outlet are closed with a mechancal switch. The device is then placed in a wet chamber at 4°C overnight to allow the probe DNAs to immobilize. During this process, the amine group of the pDNAs reacts with the succinimide group of PBASE through a conjugation reaction. After immobilization, any excess pDNAs is removed from the channel by rinsing with PBS.

After immobilizing the pDNA, it is crucial to passivate any unbound PBASE molecules to prevent nonspecific binding of target DNAs (tDNAs). This is done by flowing a 100 mM ethanolamine (NH2CH2CH2OH) solution, prepared in DI water, through the microfluidic channel for 4 hours. Ethanolamine reacts with the amine-reactive succinimide groups of the unbound PBASE molecules. Once the passivation process is complete, the device is ready for sensing and communication experiments with tDNAs.

3.5 Characterization of MC Receiver

For the electrical characterization of the fabricated devices, direct-current (DC) measurements are conducted using a high-precision source measure unit (SMU, Keysight B2902B). This SMU is connected to the device electrodes through high-impedance passive probes, as illustrated in Fig. 3.5(a).

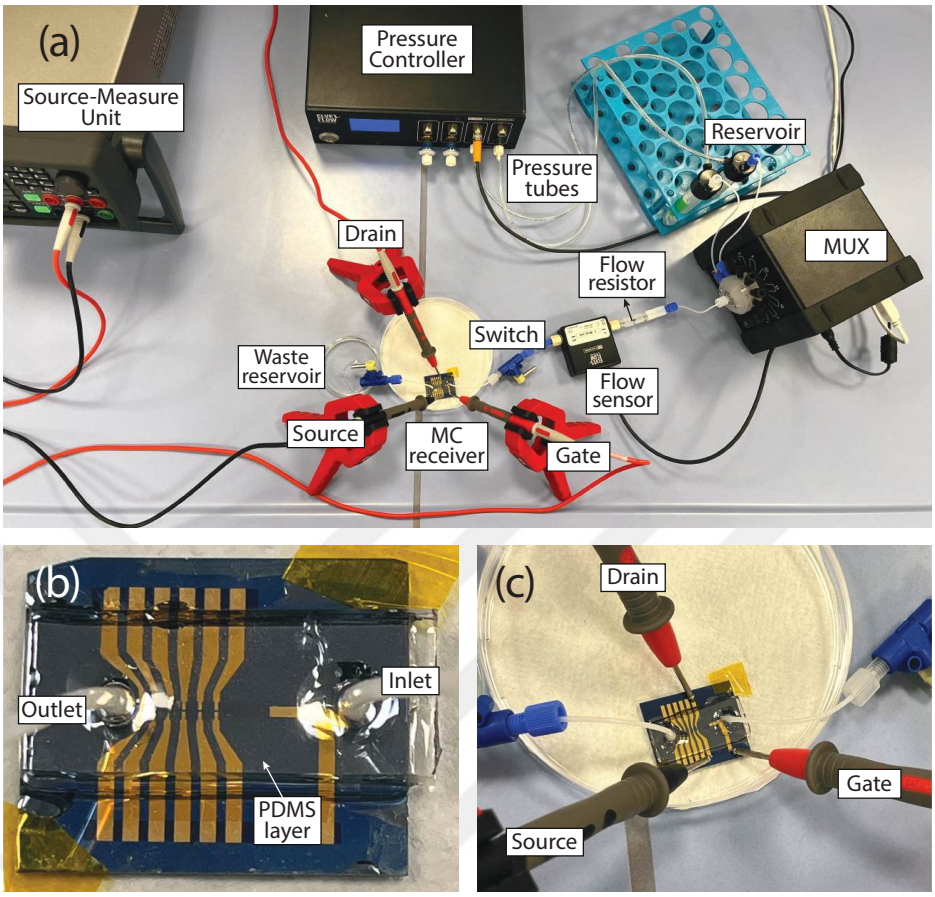

Figure 3.5: a) Microfluidic MC setup consists of a pressure controller, a high-precision source-measure unit, a flow distributor, a flow sensor, electrical probes, and various microfluidic components. b) Closer look to fabricated MC receiver bonded with PDMS channel. c) Probe connection for applying/sensing electrical voltage/current.

Transfer Characteristics

After each functionalization step, the transfer characteristics of the devices are measured using a constant drain-to-source bias of $V_{ds} = 100$ mV, with the solution gate potential V_g. The sweep rate of V_g is set at 1 mV/s. All data were collected after thoroughly rinsing the microfluidic channel and SLG surfaces with PBS to remove any excess functional molecules. This step ensures that the transfer characteristics remain unaffected by ongoing chemical reactions. PBS (pH 7.4) was used as the electrolyte for all transfer characteristic measurements. The measurements were taken from a wide range of GFETs, but the presented results belong to two different

sensors, which are displayed in Fig. 3.6 and Fig. 3.7. Fig. 3.7 primarily serves to investigate hysteresis; however, the shift in the Dirac point is also observable. Since the hysteresis in Fig. 3.6 was negligible, only the forward sweep of V_g is illustrated.

The initial measurement was taken after the microfluidic channel was filled with 1x PBS electrolyte. The ambipolar behavior of single-layer graphene (SLG) in the FET configuration was observed, along with the charge neutrality point (CNP), as can be seen in Fig 3.7(a) (or Fig. 3.6). After incubation with PBASE, a negative shift in the CNP is observed, as shown in Fig. 3.7(b) (or Fig. 3.6), which is attributed to the dominance of n-type doping from DMF, competing with the p-type doping effect of PBASE during extended incubation times [Kuscu et al., 2021]. The immobilization of pDNA led to p-type doping, causing a positive shift in the CNP, as shown in Fig. 3.7(c) (or Fig. 3.6). At pH 7.4, DNA molecules carry a negative charge, which attracts hole carriers to the graphene surface, thereby enhancing p-type doping [Kuscu et al., 2021]. The final measurements were taken after passivating the excess PBASE linkers with ethanolamine and introducing 0.01x PBS into the microfluidic channel for subsequent sensing and communication experiments. 0.01x PBS is a 100-fold diluted version of PBS using deionized (DI) water. Although ethanolamine is uncharged, the observed positive shift in the CNP indicate increased p-type doping as the ionic concentration of the buffer solution decreases. It is also important to note that a reduction in mobility was observed across all measured GFET channels after passivation with ethanolamine in 0.01x PBS. The use of the diluted PBS for sensing and communication experiments aims to reduce the impact of Debye screening, thereby improving the device's sensitivity to hybridization events on the SLG surface.

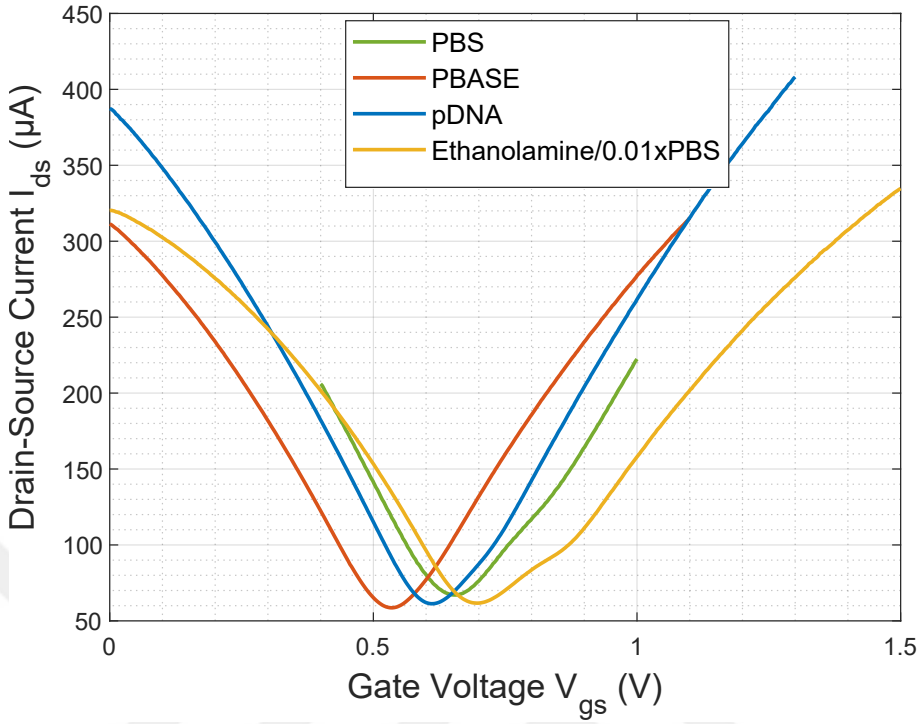

Figure 3.6: The transfer characteristics of a GFET at various stages of functionalization, represented by the drain-to-source current (I_{ds}) as a function of varying gate potential (V_{gs}) with a sweep rate of 1 mV/s. In all measurements, the drain-to-source voltage (V_{ds}) is held constant at V_{ds} =100 mV.

Hysteresis Analysis

Hysteresis in GFETs refers to the phenomenon where the transfer characteristics of the device show different behaviors during the forward and reverse sweeps of the gate voltage. This indicates that the device retains some memory of its previous state, typically caused by trapped charges, adsorbed molecules on the graphene surface or within the gate dielectric, defects in the graphene layer, or contamination during the fabrication process. The hysteresis of the fabricated GFET at various stages of functionalization is shown in Fig. 3.7. As observed, the hysteresis decreases when transitioning from the PBS to PBASE steps, and remains relatively constant during the pDNA and ethanolamine steps. The measured leakage current in samples with and without the insulating layer is shown in Fig. 3.8. As observed, the deposition of a 30 nm Al_2O_3 layer significantly suppressed the parasitic current flowing from

the gate to the source.

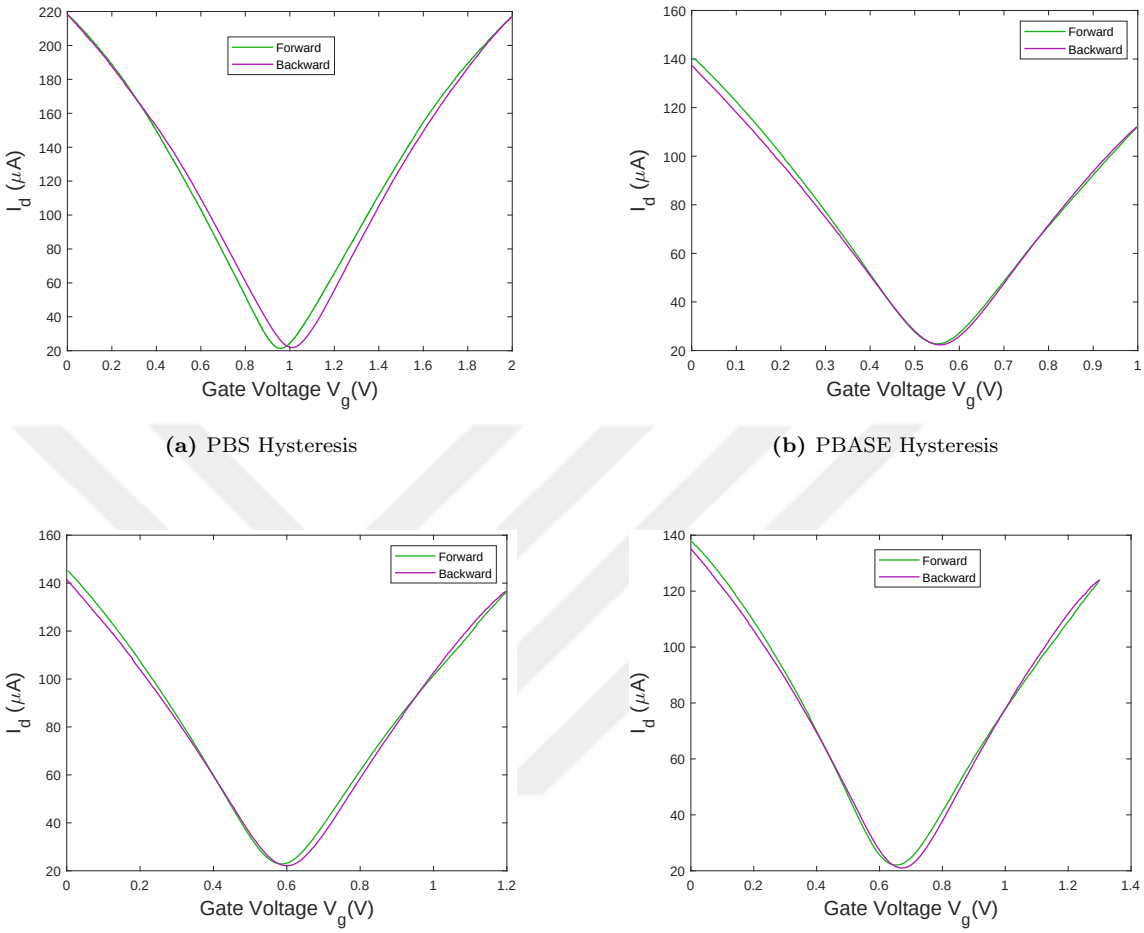

(a) PBS Hysteresis

(b) PBASE Hysteresis

(c) pDNA Hysteresis

(d) Ethanolamine Hysteresis

Figure 3.7: Transfer curve measurements for different steps of functionalisation: (a) PBS, (b) PBASE, (c) pDNA, (d) Ethanolamine.

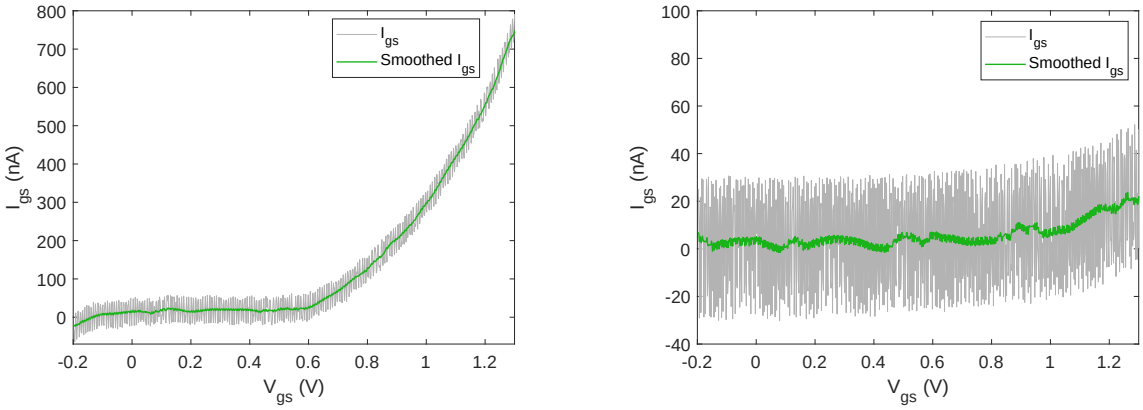

(a) Without insulator

(b) With insulator

Figure 3.8: Leakage current from the electrolyte gate to the source contact in the sensor: a) without the insulating layer, and b) with the insulating layer.

Mobility Analysis

The mobility of GFETs is an important parameter that reflects how quickly charge carriers (electrons or holes) can move through the graphene layer when an electric field is applied. Mobility is critical for assessing the performance of GFETs, especially in biosensing applications. The mobility of our receiver is calculated in back-gated configuration. Based on the linear approximation of transfer curve the mobility is calculated using the following formula

$$\mu = \frac{L}{W}\frac{t_{ox}}{\epsilon_{ox}}\frac{|g_m|}{V_{ds}} \tag{3.1}$$

where $L = 250$ μm and $W = 250$ μm represent the length and width of the graphene channels, respectively. $t_{ox} = 90$ nm and $\epsilon_{ox} = 3.4531 \times 10^{-13}$ F/cm denote the thickness and permittivity of the SiO2 layer. $V_{ds} = 100$ mV is the drain-to-source voltage, and $|g_m| = \frac{\partial I_{ds}}{\partial V_{bg}}$ represents the transconductance of the GFETs, which is calculated using a linear approximation of the transfer curve in the hole-carrier regime for the four GFET channels. The back-gated sweep of the GFETs is shown in Fig. 3.9, and the corresponding mobilities for these channels are as follows: Channel 1: 826.24 cm^2/Vs, Channel 2: 1578.75 cm^2/Vs, Channel 3: 1084.46 cm^2/Vs, and Channel 4: 1463.38 cm^2/Vs.

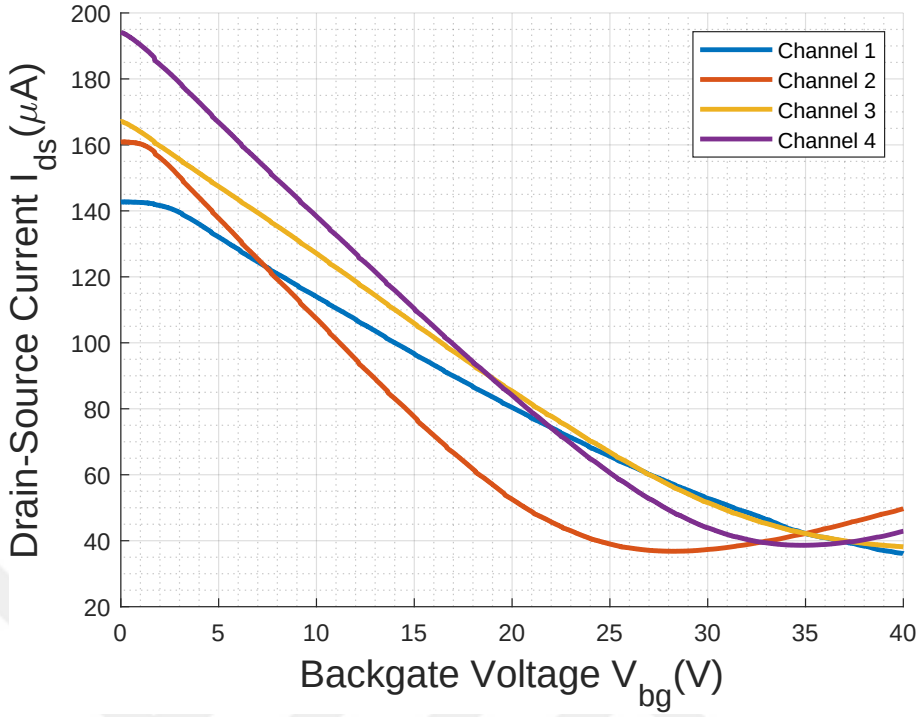

Figure 3.9: Transfer characteristics of the four graphene channels were measured in a back-gate configuration, where the back-gate voltage (V_{bg}) was swept from 0 V to 40 V in the forward direction, with the drain-source voltage (V_{ds}) set at 100 mV.

Sensing Response

To assess the sensing properties of the MC receiver, an 18-mer complementary target DNA (tDNA: 5'-ACG AAG GTC TGT AGC AAC TC-3', sourced from Sigma Aldrich) is prepared in a 0.01x PBS solution. tDNA samples with varying concentrations (ranging from 1 nM to 1 µM) are sequentially introduced into the microfluidic channel, following an order of increasing concentration. The drain-source current (Ids) is continuously measured in real-time with a drain-source voltage (Vds) of 100 mV and a gate voltage (V_g) of 0 V. Throughout the experiment, the volumetric flow rate is maintained at a constant 40 μL/min. The measurement outcomes are illustrated in Fig. 3.10, which reveals a reduction in the drain-source current when the tDNA concentration contacts the graphene following a delay time that accounts for the travel from the reservoir to the sensor surface. This indicates an n-type doping effect, as opposed to the p-type doping seen with pDNAs. As depicted in Fig. 3.10,

a higher concentration of tDNAs leads to a greater decrease in I_{ds}, indicating an increase in n-type doping.

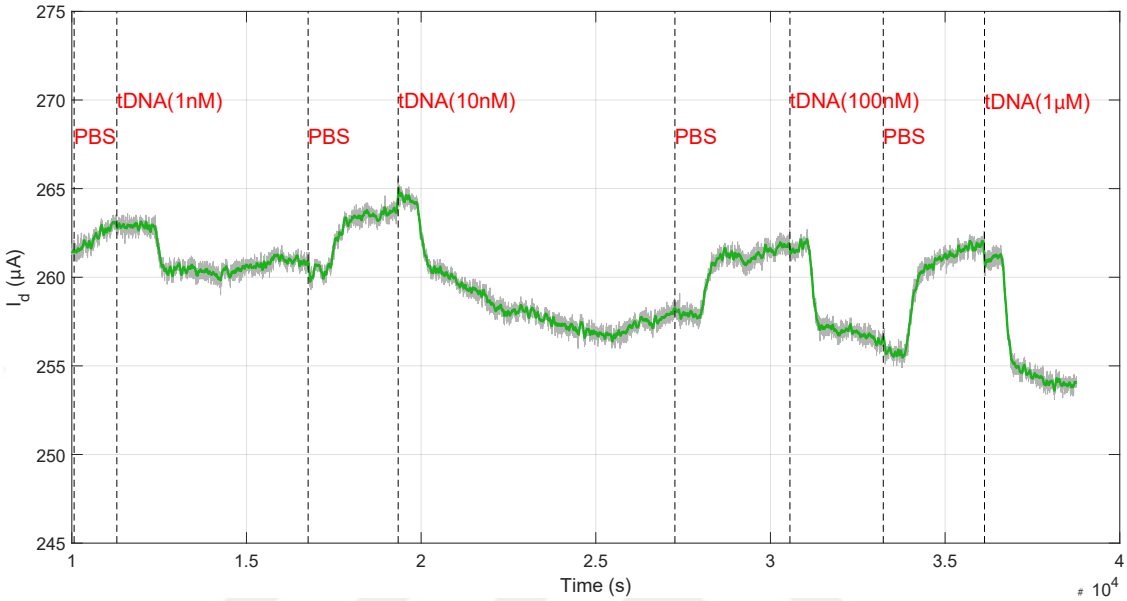

Figure 3.10: Sensor response to tDNA at various concentrations ranging from 1 nM to 1 μM, with the response strength corresponding to the tDNA concentration.

3.6 Communication Performance

The prepared testbed is ultimately used as an MC receiver to detect target information molecules in real time. To this end, two reservoirs are maintained: one containing 0.01xPBS as a buffer and the other filled with a tDNA solution prepared in 0.01xPBS as can be seen in Fig. 3.5(a). The pressure to create flow is generated by a microfludic flow controller (ElveFlow OB1 MK4), which is a flow control instrument based on piezoelectric technolgy. Both reservoirs are connected to a microfluidic flow switch distributor (ElveFLow MUX), which is used to digitally switch between solutions and is able to quickly and easily and create automated sequences of distinct solutions. To maintain a constant flow speed throughout the experiment, a microfluidic flow sensor (ElveFlow MFS) is integrated with the multiplexer. This system operates using a PID algorithm that monitors the flow rate and adjusts the pressure as needed to achieve the desired flow rate accurately and swiftly.

Time-varying Response

The time-varying response of the sensor is examined by introducing pulses of 10 nM tDNA concentration with constant and varying widths. As shown in Fig. 3.11(a), five consecutive pulses, each with a width of 1 ks, are applied to the microfluidic channels to observe the sensor's response. The association and dissociation dynamics of pDNA/tDNA molecules are tracked, with a PBS flow duration of 1.8 ks needed to return the baseline.

Fig. 3.11(b) presents six 10 nM tDNA pulses with progressively decreasing widths: T_p = 1 ks, 500 s, 250 s, 125 s, 62 s, and 32 s. The PBS flow duration after each pulse remains constant at 1.3 ks. As T_p decreases, the reduction in I_{ds} becomes less pronounced, and the current returns to baseline more quickly after shorter pulses. This behavior suggests potential improvements in detection time and data rate in a communication scenario.

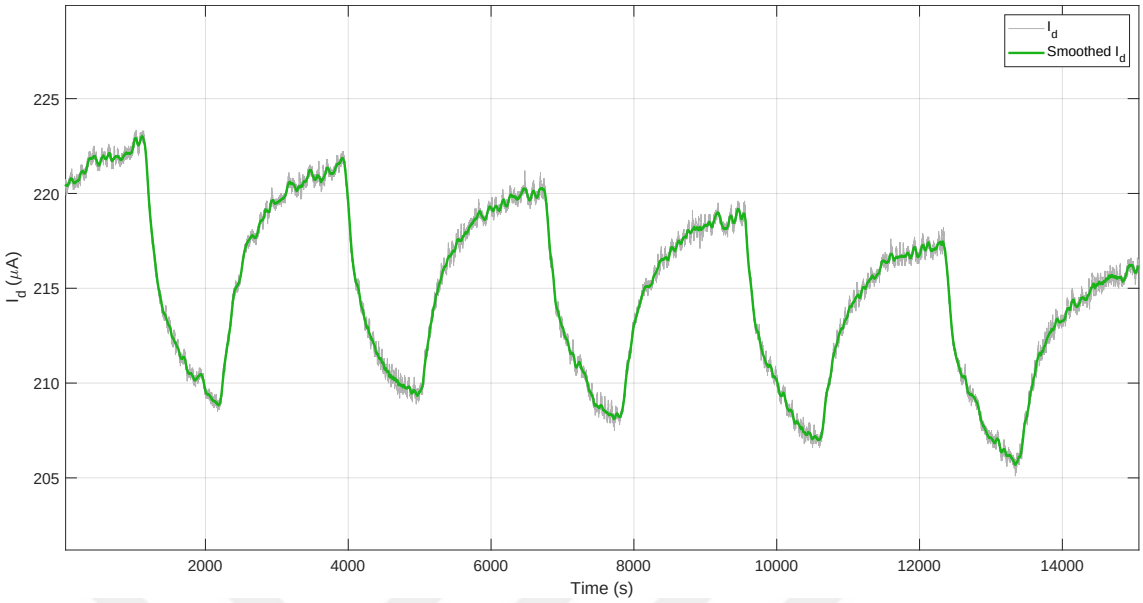

(a)

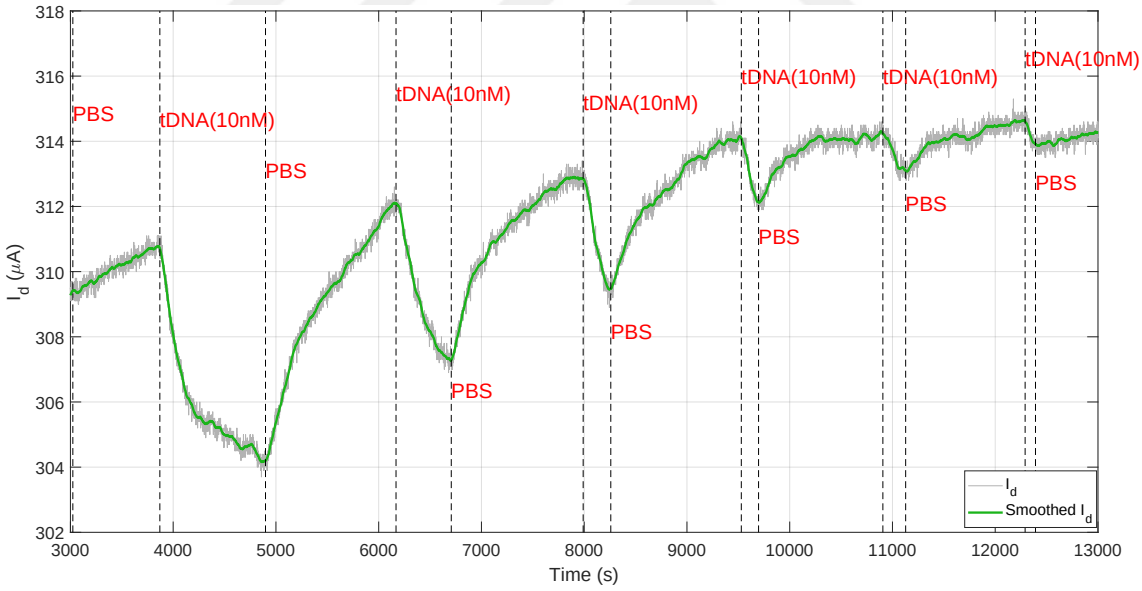

(b)

Figure 3.11: a) Sensor response to 10 nM tDNA pulses with a constant pulse width of 1 ks, followed by a PBS duration of 1.8 ks after each tDNA pulse. b) Sensor response to 10 nM tDNA pulses with varying pulse widths, ranging from 1 ks to 32 s, and a constant PBS duration of 1.3 ks.

Inter Symbol Interference

Molecular communication often grapples with the issue of Inter Symbol Interference (ISI). This occurs because, due to the nature of diffusion, some molecules fail to reach the receiver within their allotted time slots. These late arrivals extend the signal's tail, causing interference with subsequent transmissions and potentially leading to incorrect signal detection. To mitigate ISI, one effective approach is to extend the symbol duration, which gives molecules additional time to reach their intended destinations and reduces the presence of residual molecules in the channel. However, while this method can reduce ISI, it also diminishes the data rate, which is typically slower in diffusion-based molecular communication systems [Tepekule et al., 2015, Chang et al., 2017]. Fig. 3.12 presents the ISI analysis in our MC system. In this figure, multiple pulses with a constant width of $T_p = 250$ s are introduced into the microfluidic channel, while the PBS flow duration required to restore the baseline is progressively reduced. As observed, the current does not fully return to baseline as the PBS duration decreases. Beyond a certain point ($T_{PBS} = 37$ s in the setup), it becomes increasingly difficult to distinguish between successive tDNA pulses.

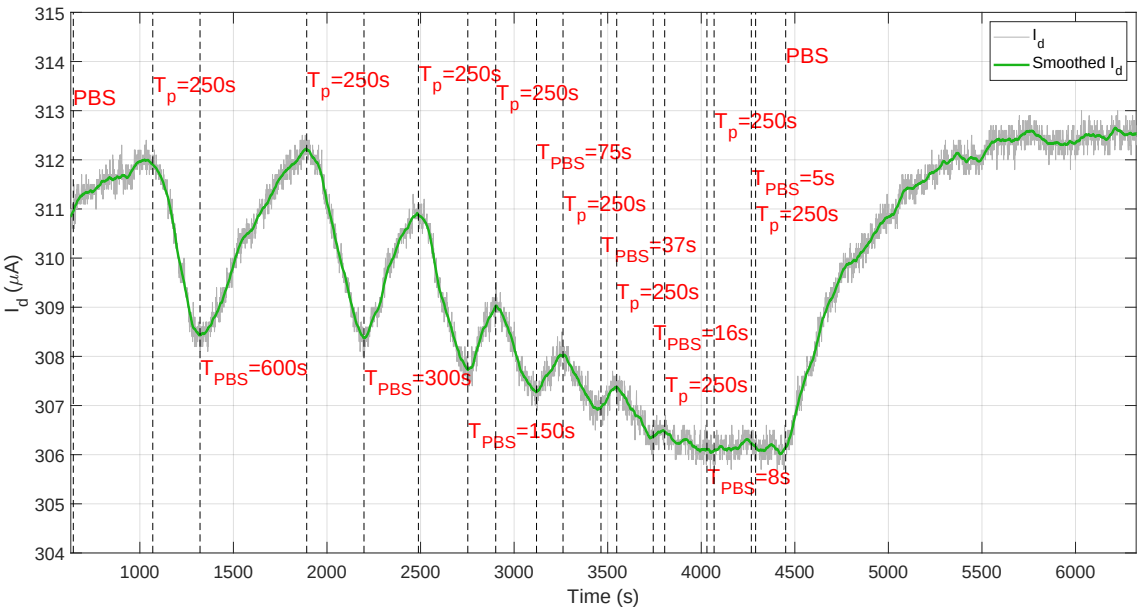

Figure 3.12: ISI analysis of the sensor using 10 nM tDNA pulses with a constant pulse width and varying PBS durations ranging from 600 s to 5 s.

Data Transmission

For evaluating the detection method and the performance of a graphene bioFET-based molecular communication receiver, a 10-bit pseudorandom binary sequence is encoded into tDNA concentrations and transmitted through a microfluidic channel. The fabricated MC receiver, positioned at the bottom of the channel, detects the transmitted sequence. In this part, a bit value of 1 is indicated by a pulse at a concentration of 10 nM and 100nM, while a bit value of 0 is represented by the absence of any pulse transmission throughout the entire bit interval, meaning the buffer line remains connected to the microfluidic channel. The results are presented for varying bit intervals. As anticipated, the slow dissociation rate of the bound tDNAs from the immobilized pDNAs leads to significant ISI, which can complicate decoding at the receiver. This ISI is more pronounced with shorter bit intervals, or higher transmission rates, as the baseline does not have sufficient time to recover. Conversely, with a bit interval, ISI is considerably reduced, allowing Ids to return to the baseline.

Another key observation is that the propagation delay (t_{delay}) between the transmission of a bit-1 and the receiver's response remains consistently around 160 seconds for a flow rate of u = 40 µL/min and 80 seconds for u = 80 µL/min. This delay stays nearly constant throughout the entire data transmission period. These findings suggest that applying a fixed delay shift to the receiver's response could effectively synchronize the receiver with the transmitter during decoding.

The communication scenarios is illustrated in Fig. 3.13. Considering the observation of a constant delay during data transmission, the delay-adjusted bit intervals are represented by dashed lines in Fig. 3.13, with the transmitted bits labeled within each corresponding bit interval. In the data transmission cycle depicted in Fig. 3.13(a), the parameters are set to T_p = 60 s, T_s = 150 s, u = 40 µL/min, and a concentration of 10 nM. A decrease in I_{ds} is observed for bit-1, while an increase occurs for bit-0. In other words, the slope of the curve becomes negative for bit-1 and non-negative for bit-0. A pre-equilibrium detection method will be implemented later to accurately detect the transmitted symbol, relying on the slope of I_{ds} from

the time of symbol transmission $t_{transmit}$, plus the propagation delay t_{delay}, up to the pulse width T_p. Since PBS flows at $t = t_{transmit} + t_{delay} + T_p$ in all transmitted symbols, the slope of I_{ds} across the entire symbol interval T_s is not considered. While this poses no issue when transmitting bit-0, it becomes critical during bit-1 transmission, where a change in slope is expected. Therefore, the slope of I_{ds} in the range $t_{transmit} + t_{delay} \leq t \leq T_p$ is of particular interest. For the purpose of this thesis, the detection of transmitted symbols relies on comparing two points: $t_{transmit} + t_{delay}$ and $t_{transmit} + t_{delay} + T_p$. However, the pre-equilibrium technique will be thoroughly investigated and presented in a separate paper.

In the transmission cycle shown in Fig. 3.13(b), the parameters are the same as those in Fig. 3.13(a), with the only change being a reduction in T_p from 60 s to 30 s. As observed, the received signal can still be detected with acceptable accuracy. However, the magnitude of the decrease/increase in I_{ds} during the symbol interval is reduced.

The result shown in Fig. 3.13(c) is obtained using the same parameter values as in Fig. 3.13(b), with the only change being an increase in flow rate from 40 µL/min to 80 µL/min. As observed, the higher flow rate improves signal detection, making the difference in I_{ds} more distinguishable. This is primarily due to a greater number of molecules being introduced into the channel within the given time, leading to more hybridization with pDNAs. However, this effect is expected to diminish as the flow rate continues to increase beyond a certain point, as excessively high flow rates could cause tDNA molecules to pass through the channel too quickly, preventing sufficient binding to pDNAs for hybridization. Another important observation is the reduction in propagation delay, t_{delay}, from 160 seconds to 80 seconds, which aligns with our expectations.

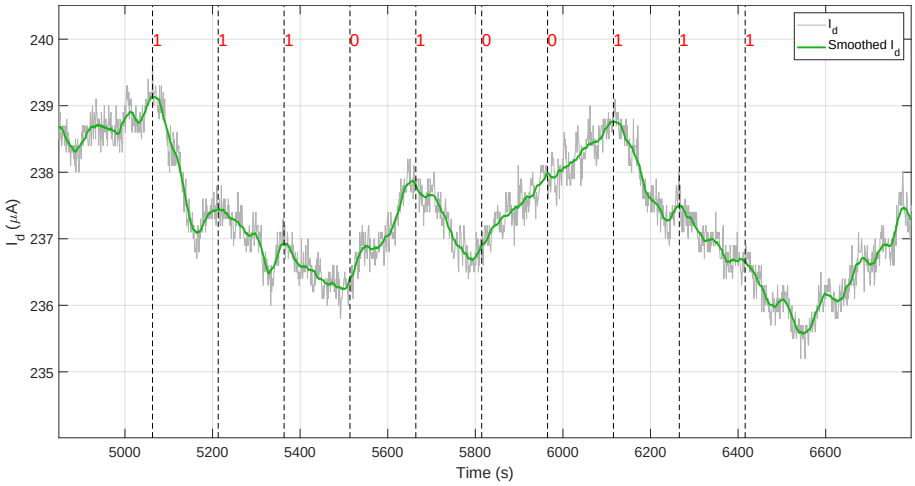

(a) T_p =60s, T_s = 150s, u =40 μL/min, C_{tDNA}=10nM

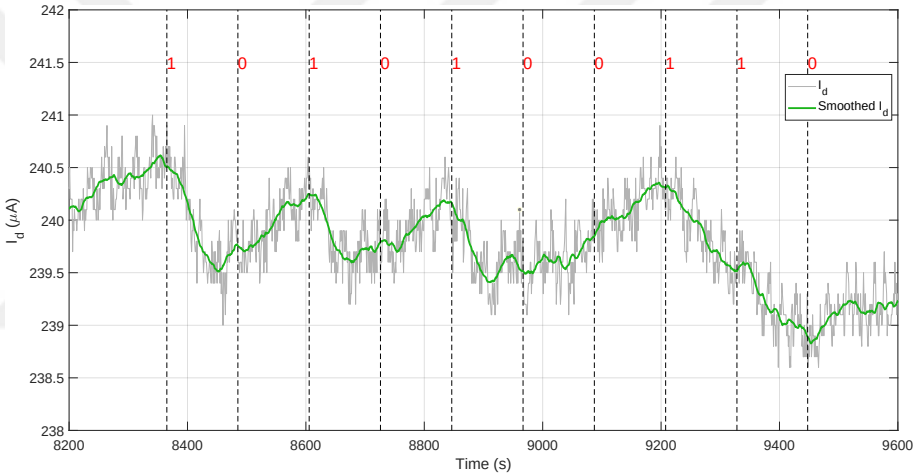

(b) T_p =30s, T_s = 120s, u =40 μL/min, C_{tDNA}=10nM

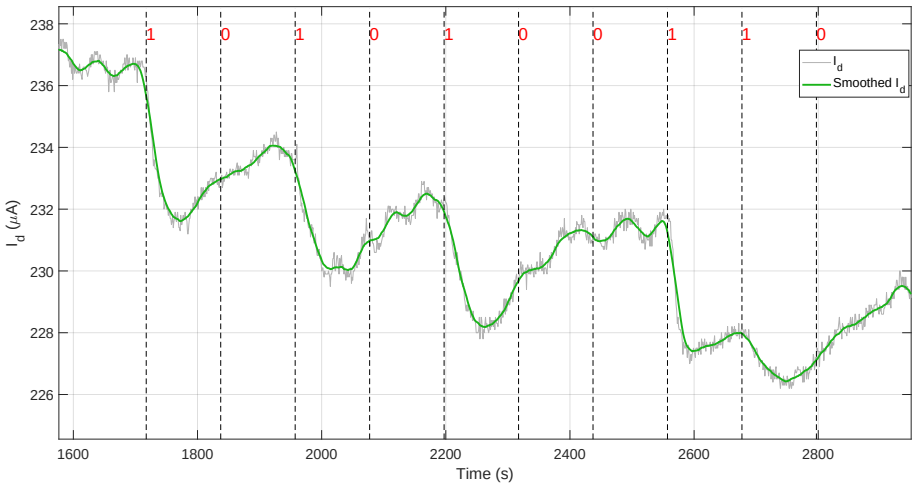

(c) T_p =60s, T_s = 150s, u =80 μL/min, C_{tDNA}=10nM

Figure 3.13: Data transmission cycles utilizing 10nM tDNA molecules, with one parameter varied at a time.

The data transmission shown in Fig. 3.14(a) is obtained from a different sensor, with parameters set to $T_p = 60$ s, $T_s = 150$ s, $u = 80$ µL/min, and a concentration of 100 nM. The concentration was increased due to this sensor's lower sensitivity compared to the previous one. In Fig. 3.14(b), T_p is reduced to 30 s. As observed, although the magnitude of I_{ds} fluctuations in response to the detected symbols decreases, the bits can still be extracted with acceptable accuracy. In the data transmission results shown in Fig. 3.15(a), T_s is reduced to 90 seconds while all other parameters, including T_p, remain the same as in Fig. 3.14(b). This reduction shortens the PBS duration following T_p, leading to increased ISI and complicating symbol detection, resulting in a 10% bit error rate (BER). Finally, in the results shown in Fig. 3.15(b), T_p is reduced to 20 seconds while the other parameters remain the same as in Fig. 3.15(a). This adjustment leads to a further increase in BER during data transmission by erroneously transmitting an additional bit. Overall, this set of parameters remains susceptible to external noise and ISI. Consequently, the optimal parameters for communication are identified as $T_p = 60$ s, $T_s = 150$ s, $u = 80$ µL/min, and a concentration of 100 nM.

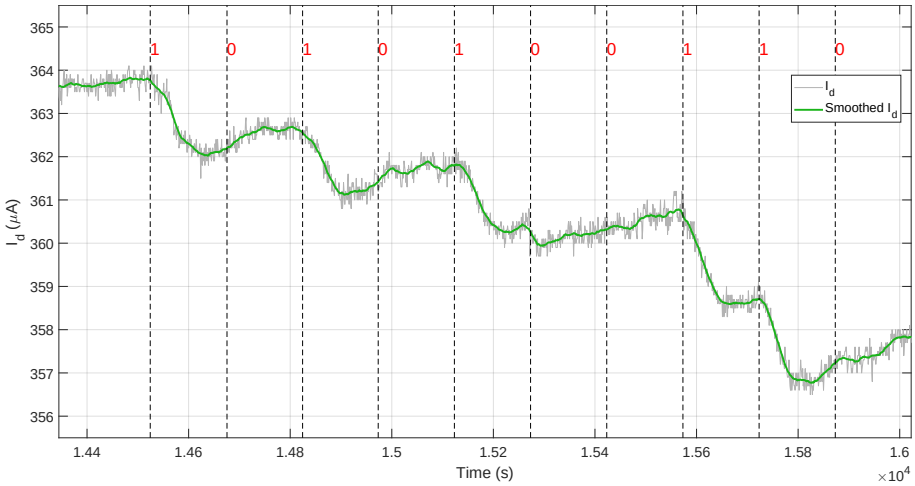

(a) T_p =60s, T_s = 150s, u =80 μL/min, C_{tDNA}=100nM

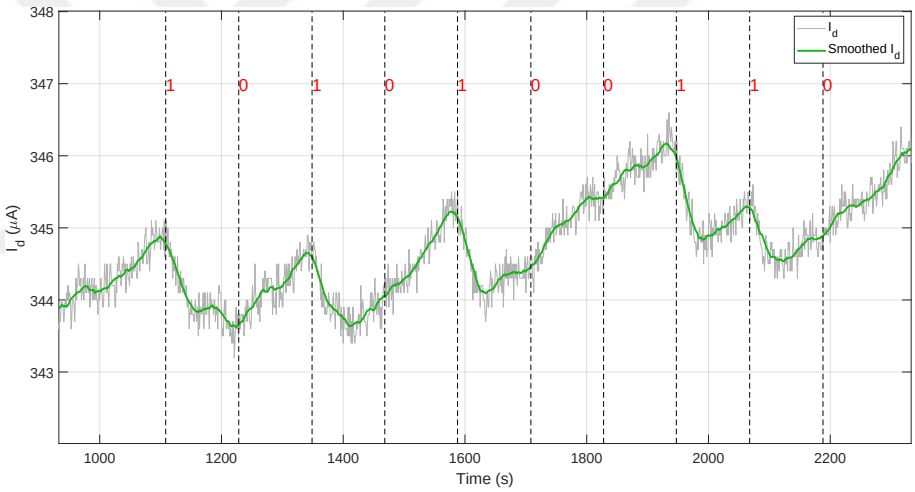

(b) T_p =30s, T_s = 120s, u =80 μL/min, C_{tDNA}=100nM

Figure 3.14: Data transmission cycles employing 100 nM tDNA molecules, with a single parameter varied at a time.

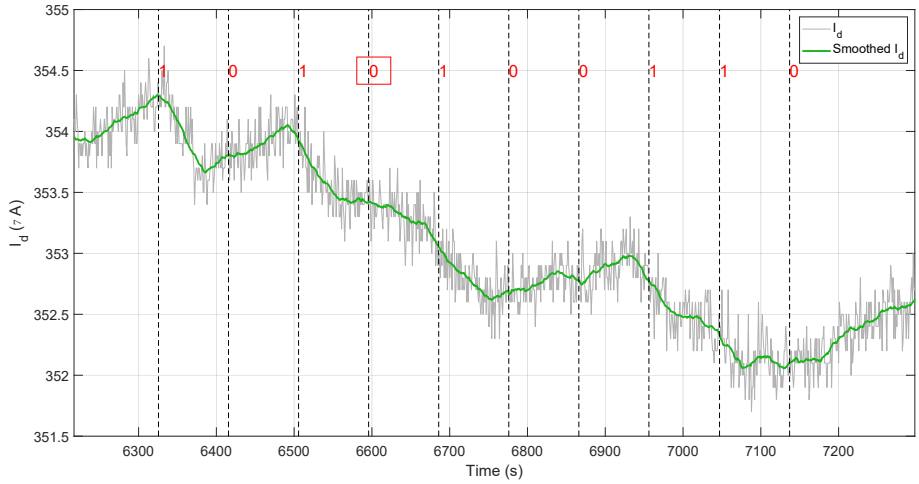

(a) T_p =30s, T_s = 90s, u =80 μL/min, C_{tDNA}=100nM

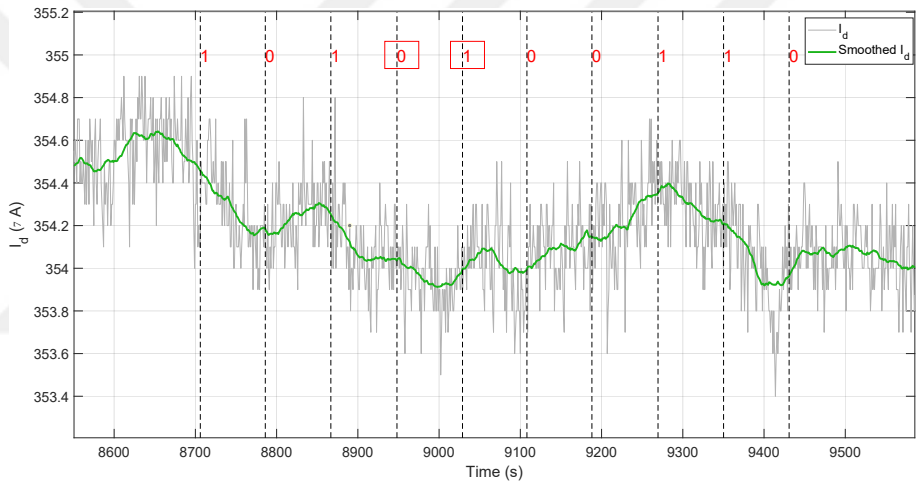

(b) T_p =20s, T_s = 80s, u =80 μL/min, C_{tDNA}=100nM

Figure 3.15: Data transmission cycles employing 100 nM tDNA molecules, with a single parameter adjusted at a time.

Chapter 4

CONCLUSION

In this thesis, I addressed the challenges associated with molecular communication (MC) by focusing on the design, modeling, simulation, fabrication, and characterization of MC systems. I developed an analytical model for a graphene bioFET-based MC receiver and a microfluidic propagation channel. The accuracy of the proposed model was validated through particle-based spatial stochastic simulations. Additionally, I fabricated a graphene bioFET-based DNA sensor to function as an MC receiver and integrated it into a microfluidic MC system for data transmission.

Molecular communication has been extensively explored in the time domain due to the unique nature of its information carriers, namely discrete molecules, which create complexities and ambiguities in defining carrier waves and frequencies for this unconventional communication method. Moreover, the inherent nonlinearity and time-varying characteristics of MC systems present obstacles to the application of frequency-domain techniques, which are commonly used in other areas of communication research. However, when MC systems can be approximated as linear and time-invariant (LTI), frequency-domain analysis becomes valuable for understanding key channel characteristics such as bandwidth, signal dispersion, and distortion. This approach also sheds light on how system parameters, like channel geometry, ligand-receptor binding kinetics, and the electrical properties of the receiver's transducer, affect communication performance. In this thesis, I developed a modular analytical model for the three key components of a MC system: the propagation channel, ligand-receptor interactions, and receiver transduction. Additionally, the influence of various system parameters on the performance and behavior of the MC system was thoroughly investigated.

MC literature is tremendously overwhelmed with theoretical models that rely on unrealistic and physically irrelevant assumptions, often treating MC components

in isolation and neglecting the crucial physical processes occurring at the interfaces between these components. To overcome this limitation, I present the design, fabrication, and characterization of a graphene FET-based DNA-selective receiver in micro/nanoscale dimension. The receiver's detection performance was evaluated using a PDMS-based microfluidic testbed. Binary information, encoded in the concentration of target DNA molecules, was transmitted at varying rates to assess the system's capabilities.

The practical optimised receiver architectures developed in this thesis aim to address the significant gap between theory and practice in molecular communication. This gap has long hindered progress and innovation in the field, especially with regard to groundbreaking applications. These advancements will help overcome this major bottleneck.

BIBLIOGRAPHY

[Akan et al., 2016] Akan, O. B., Ramezani, H., Khan, T., Abbasi, N. A., and Kuscu, M. (2016). Fundamentals of molecular information and communication science. *Proceedings of the IEEE*, 105(2):306–318.

[Aktas and Akan, 2022] Aktas, D. and Akan, O. B. (2022). Weight shift keying (wsk) with practical mechanical receivers for molecular communications in internet of everything. *IEEE Journal on Selected Areas in Communications*, 40(11):3285–3294.

[Akyildiz et al., 2008] Akyildiz, I. F., Brunetti, F., and Blázquez, C. (2008). Nanonetworks: A new communication paradigm. *Computer Networks*, 52(12):2260–2279.

[Akyildiz et al., 2020] Akyildiz, I. F., Ghovanloo, M., Guler, U., Ozkaya-Ahmadov, T., Sarioglu, A. F., and Unluturk, B. D. (2020). Panacea: An internet of bio-nanothings application for early detection and mitigation of infectious diseases. *IEEE Access*, 8:140512–140523.

[Akyildiz et al., 2011] Akyildiz, I. F., Jornet, J. M., and Pierobon, M. (2011). Nanonetworks: A new frontier in communications. *Communications of the ACM*, 54(11):84–89.

[Akyildiz et al., 2015] Akyildiz, I. F., Pierobon, M., Balasubramaniam, S., and Koucheryavy, Y. (2015). The internet of bio-nano things. *IEEE Communications Magazine*, 53(3):32–40.

[Andrews, 2017] Andrews, S. S. (2017). Smoldyn: particle-based simulation with rule-based modeling, improved molecular interaction and a library interface. *Bioinformatics*, 33(5):710–717.

[Barsoukov and Macdonald, 2005] Barsoukov, E. and Macdonald, J. R. (2005). Impedance spectroscopy theory, experiment, and. *Applications, 2nd ed.(Hoboken, NJ: John Wiley &Sons, Inc., 2005).*

[Bicen and Akyildiz, 2013] Bicen, A. O. and Akyildiz, I. F. (2013). System-theoretic analysis and least-squares design of microfluidic channels for flow-induced molecular communication. *IEEE Transactions on Signal Processing*, 61(20):5000–5013.

[Bolhassan et al., 2023] Bolhassan, I. M., Abdali, A., and Kuscu, M. (2023). Microfluidic molecular communication transmitter based on hydrodynamic gating. *arXiv preprint.*

[Chang et al., 2017] Chang, G., Lin, L., and Yan, H. (2017). Adaptive detection and isi mitigation for mobile molecular communication. *IEEE Transactions on nanobioscience*, 17(1):21–35.

[Chazalviel, 1999] Chazalviel, J.-N. (1999). *Coulomb screening by mobile charges: applications to materials science, chemistry, and biology.* Springer Science & Business Media.

[Civas et al., 2023a] Civas, M., Abdali, A., Kuscu, M., and Akan, O. B. (2023a). Frequency-domain detection for molecular communications. *Proceedings of IEEE International Confrence on Communication (ICC).*

[Civas et al., 2023b] Civas, M., Kuscu, M., Cetinkaya, O., Ortlek, B. E., and Akan, O. B. (2023b). Graphene and related materials for the internet of bio-nano things. *in print, APL Materials.*

[Deng et al., 2017] Deng, Y., Pierobon, M., and Nallanathan, A. (2017). A microfluidic feed forward loop pulse generator for molecular communication. In *GLOBECOM 2017-2017 IEEE Global Communications Conference*, pages 1–7. IEEE.

[Garcia-Cortadella et al., 2020] Garcia-Cortadella, R., Masvidal-Codina, E., De la Cruz, J. M., Schäfer, N., Schwesig, G., Jeschke, C., Martinez-Aguilar, J., Sanchez-Vives, M. V., Villa, R., Illa, X., et al. (2020). Distortion-free sensing of neural activity using graphene transistors. *Small*, 16(16):1906640.

[Garrison et al., 2018] Garrison, J., Li, Z., Palanisamy, B., Wang, L., and Seker, E. (2018). An electrically-controlled programmable microfluidic concentration waveform generator. *Journal of biological engineering*, 12(1):1–10.

[Hsu and Mansfeld, 2001] Hsu, C. and Mansfeld, F. (2001). Concerning the conversion of the constant phase element parameter y0 into a capacitance. *Corrosion*, 57(09).

[Huang et al., 2021a] Huang, Y., Ji, F., Wei, Z., Wen, M., Chen, X., Tang, Y., and Guo, W. (2021a). Frequency domain analysis and equalization for molecular communication. *IEEE Transactions on Signal Processing*, 69:1952–1967.

[Huang et al., 2021b] Huang, Y., Ji, F., Wen, M., Tang, Y., Chen, X., and Guo, W. (2021b). A frequency domain view on diffusion-based molecular communication channels. In *ICC 2021-IEEE International Conference on Communications*, pages 1–6. IEEE.

[Jamali et al., 2019] Jamali, V., Ahmadzadeh, A., Wicke, W., Noel, A., and Schober, R. (2019). Channel modeling for diffusive molecular communication—a tutorial review. *Proceedings of the IEEE*, 107(7):1256–1301.

[Khademi and Barz, 2020] Khademi, M. and Barz, D. P. (2020). Structure of the electrical double layer revisited: Electrode capacitance in aqueous solutions. *Langmuir*, 36(16):4250–4260.

[Kuscu and Akan, 2016a] Kuscu, M. and Akan, O. B. (2016a). Modeling and analysis of sinw fet-based molecular communication receiver. *IEEE Transactions on Communications*, 64(9):3708–3721.

[Kuscu and Akan, 2016b] Kuscu, M. and Akan, O. B. (2016b). On the physical design of molecular communication receiver based on nanoscale biosensors. *IEEE Sensors Journal*, 16(8):2228–2243.

[Kuscu and Akan, 2018] Kuscu, M. and Akan, O. B. (2018). Modeling convection-diffusion-reaction systems for microfluidic molecular communications with surface-based receivers in internet of bio-nano things. *PloS One*, 13(2):e0192202.

[Kuscu and Akan, 2019] Kuscu, M. and Akan, O. B. (2019). Channel sensing in molecular communications with single type of ligand receptors. *IEEE Transactions on Communications*, 67(10):6868–6884.

[Kuscu et al., 2019] Kuscu, M., Dinc, E., Bilgin, B. A., Ramezani, H., and Akan, O. B. (2019). Transmitter and receiver architectures for molecular communications: A survey on physical design with modulation, coding, and detection techniques. *Proceedings of the IEEE*, 107(7):1302–1341.

[Kuscu et al., 2021] Kuscu, M., Ramezani, H., Dinc, E., Akhavan, S., and Akan, O. B. (2021). Fabrication and microfluidic analysis of graphene-based molecular communication receiver for internet of nano things (iont). *Scientific Reports*, 11(1):1–20.

[Lauffenburger and Linderman, 1996] Lauffenburger, D. A. and Linderman, J. (1996). *Receptors: models for binding, trafficking, and signaling.* Oxford University Press.

[Lindgren et al., 2019] Lindgren, E. B., Quan, C., and Stamm, B. (2019). Theoretical analysis of screened many-body electrostatic interactions between charged polarizable particles. *The Journal of chemical physics*, 150(4).

[Marzo et al., 2019] Marzo, J. L., Jornet, J. M., and Pierobon, M. (2019). Nanonetworks in biomedical applications. *Current drug targets*, 20(8):800–807.

[Pal et al., 2021] Pal, S., Islam, N., and Misra, S. (2021). Vivid: In vivo end-to-end molecular communication model for covid-19. *IEEE Transactions on Molecular, Biological and Multi-Scale Communications*, 7(3):142–152.

[Pierobon and Akyildiz, 2010] Pierobon, M. and Akyildiz, I. F. (2010). A physical end-to-end model for molecular communication in nanonetworks. *IEEE Journal on Selected Areas in Communications*, 28(4):602–611.

[Pierobon and Akyildiz, 2011a] Pierobon, M. and Akyildiz, I. F. (2011a). Diffusion-based noise analysis for molecular communication in nanonetworks. *IEEE Transactions on signal processing*, 59(6):2532–2547.

[Pierobon and Akyildiz, 2011b] Pierobon, M. and Akyildiz, I. F. (2011b). Noise analysis in ligand-binding reception for molecular communication in nanonetworks. *IEEE Transactions on Signal Processing*, 59(9):4168–4182.

[Rajan et al., 2013] Rajan, N. K., Duan, X., and Reed, M. A. (2013). Performance limitations for nanowire/nanoribbon biosensors. *Wiley Interdisciplinary Reviews: Nanomedicine and Nanobiotechnology*, 5(6):629–645.

[ShahMohammadian et al., 2013] ShahMohammadian, H., Messier, G. G., and Magierowski, S. (2013). Modelling the reception process in diffusion-based molecular communication channels. In *2013 IEEE International Conference on Communications Workshops (ICC)*, pages 782–786. IEEE.

[Stojek, 2010] Stojek, Z. (2010). The electrical double layer and its structure. *Electroanalytical methods: Guide to experiments and applications*, pages 3–9.

[Stylianopoulos et al., 2010] Stylianopoulos, T., Poh, M.-Z., Insin, N., Bawendi, M. G., Fukumura, D., Munn, L. L., and Jain, R. K. (2010). Diffusion of particles in the extracellular matrix: the effect of repulsive electrostatic interactions. *Biophysical journal*, 99(5):1342–1349.

[Sun and Liu, 2019] Sun, J. and Liu, Y. (2019). Unique constant phase element behavior of the electrolyte–graphene interface. *Nanomaterials*, 9(7):923.

[Tepekule et al., 2015] Tepekule, B., Pusane, A. E., Yilmaz, H. B., Chae, C.-B., and Tugcu, T. (2015). Isi mitigation techniques in molecular communication. *IEEE Transactions on Molecular, Biological, and Multi-Scale Communications*, 1(2):202–216.

[Unluturk and Akyildiz, 2016] Unluturk, B. D. and Akyildiz, I. F. (2016). An end-to-end model of plant pheromone channel for long range molecular communication. *IEEE transactions on nanobioscience*, 16(1):11–20.

[Walter et al., 2023] Walter, V., Bi, D., Salehi-Reyhani, A., and Deng, Y. (2023). Real-time signal processing via chemical reactions for a microfluidic molecular communication system. *Nature Communications*, 14(1):7188.

[Wang et al., 2014] Wang, S., Guo, W., and McDonnell, M. D. (2014). Transmit pulse shaping for molecular communications. In *2014 IEEE Conference on Computer Communications Workshops (INFOCOM WKSHPS)*, pages 209–210. IEEE.

[Xu et al., 2011] Xu, H., Zhang, Z., Xu, H., Wang, Z., Wang, S., and Peng, L.-M. (2011). Top-gated graphene field-effect transistors with high normalized transconductance and designable dirac point voltage. *ACS Nano*, 5(6):5031–5037.

[Xu et al., 2017] Xu, S., Zhan, J., Man, B., Jiang, S., Yue, W., Gao, S., Guo, C., Liu, H., Li, Z., Wang, J., et al. (2017). Real-time reliable determination of binding kinetics of dna hybridization using a multi-channel graphene biosensor. *Nature Communications*, 8(1):14902.

[Zadeh et al., 2023] Zadeh, M. K., Bolhassan, I. M., and Kuscu, M. (2023). Microfluidic pulse shaping methods for molecular communications. *Nano Communication Networks*, page 100453.